

Supporting Information for

Assessing the Influence of Void Environment in MFI Zeolites on Propene Oligomerization Kinetics Using a Combined Computational and Experimental Approach

Lauren Kilburn,^{1,2} Diamarys Salome Rivera,¹ Elizabeth E. Bickel Rogers,¹ Rajamani Gounder,^{*,1}

David D. Hibbitts^{*,1,2}

*¹Charles D. Davidson School of Chemical Engineering, Purdue University, 480 Stadium Mall
Drive, West Lafayette, IN 47907, USA*

²Department of Chemical Engineering, University of Florida, Gainesville, FL 32611, USA

*Corresponding authors. E-mails: rgounder@purdue.edu, hibbitts@purdue.edu

Table of Contents

S1. Synthesis of MFI Zeolites	4
<i>S1.1 MFI synthesis using TPA⁺</i>	4
<i>S1.2 MFI synthesis using EDA and TPA⁺</i>	5
<i>S1.3 MFI synthesis using DABCO and MA</i>	5
<i>S1.4 TON synthesis with varied ISDA/OSDA</i>	6
S2. Characterization of Zeolites	7
<i>S2.1 X-Ray Diffraction Patterns on MFI and TON zeolites</i>	7
<i>S2.2 N₂ Adsorption Isotherms on MFI and TON zeolites</i>	9
<i>S2.3 Temperature Programmed Desorption Profiles for NH₄-Form Zeolite Samples</i>	11
<i>S2.4 Elemental Composition and Cobalt Titration</i>	13
<i>S2.5 Scanning Electron Microscopy (SEM) images for MFI and TON samples</i>	13
S3. Propene Oligomerization Kinetic Measurements	17
S4. MFI Framework Details	18
S6. Temperature-Corrected Entropy and Enthalpy Calculations	20
S7. Deprotonation Energies (DPE) per O-site	20
S8. Adsorption Free Energy of C₃ species at Each O-site	22
S9. Adsorption Free Energy of Most Stable C₃ Adsorbate at Each O-site	23
S10. Binding Free Energy of C₃ Adsorbates at Each T-site	24
S11. Images of C₃ Adsorbates at Each T-site	25
S12. H-bonded C₆ Thermochemical Cycle	37
S13. Images of C₆ H-bonded Alkenes at Each T-site	38
S14. Propene Dimerization Transition State Structure	44
S15. Images of Transition State at Each T-site	47
S16. Second Order Effective Free Energy Barriers	51
S17. Propene Dimerization Transition State Thermochemical Cycle	52

S18. Acid Site Distortion and Adsorbate-Acid Site Interaction Distance	53
S19. Propene Dimerization Step Pressure and Step Temperature Experiments	54
S20. Analysis of Product Selectivity Between MFI Samples of Different H⁺-site Location	55

S1. Synthesis of MFI Zeolites

S1.1 MFI synthesis using TPA⁺

The MFI-TPA samples used in this study were reported in a previous publication.¹ In the previous publication, the sample naming convention was MFI-X-Y where 'X' is the approximate H⁺/unit cell (u.c.) and Y is the mean crystallite size estimated by Scanning Electron Microscopy (SEM). The MFI-TPA-0.33 sample was prepared using a synthesis gel with molar ratios of 1 SiO₂/0.009 Al₂(SO₄)₃/0.078 NaOH/0.18 TPAOH/29 H₂O. The synthesis gel was prepared by mixing 14.5 g of tetrapropylammonium hydroxide solution (TPAOH, Alfa Aesar 40 wt/wt % in H₂O), 4.91 g of sodium hydroxide solution (NaOH, Sigma-Aldrich, 97 wt%, 10 wt/wt% in deionized H₂O (18.2 MΩ)), and 58.8 g of deionized H₂O and stirred until homogenized in a perfluoroalkoxy alkane (PFA) jar. In a separate PFA jar, 0.952 g of aluminum sulfate octadecahydrate (Al₂(SO₄)₃ · 18 H₂O, Sigma-Aldrich, ≥ 97%) was dissolved in 10g of deionized H₂O and added dropwise to the first solution of TPAOH, NaOH and H₂O. Lastly, 32.7 g of tetraethyl orthosilicate (TEOS, Aldrich, 98%) was added to the mixture and stirred for 24 h under ambient conditions. After, the synthesis solution was transferred to a 45 mL Teflon-lined stainless-steel autoclave in a forced convection oven at 443 K for 24 h under rotation (60rpm).

For MFI-TPA-0.06 a synthesis gel was prepared with molar ratios of 1 SiO₂/0.010 Al₂(SO₄)₃/0.092 NaOH/0.25 TPAOH/13 H₂O. The synthesis gel was prepared by combining 31.8 g of TPAOH (Alfa Aesar 40 wt/wt % in H₂O), 0.92g of NaOH (Sigma-Aldrich, 97 wt%), and 26.4 g of deionized water and stirred until homogenized in a PFA jar. In a separate PFA jar, 1.67 g of Al₂(SO₄)₃ · 18H₂O (Sigma-Aldrich, ≥ 97%) was dissolved in 10 g of deionized H₂O and added dropwise to the first solution. After, 52.1 g of TEOS (Aldrich, 98%) was added to the mixture and stirred for 24 h under 353 K. The synthesis solution was then transferred to a 45mL Teflon-lined stainless-steel autoclave in a forced convection oven at 443 K for 24 h under rotation (60rpm).

The MFI-C₆₆₆-0.03 was synthesized with a gemini-type quaternary ammonium surfactant (C₆₆₆, C₆H₁₃-N⁺(CH₃)₂-C₆H₁₂-N⁺(CH₃)₂-C₆H₁₂ · 2Br⁻) that was prepared by following previously reported methods.² The synthesis gel was prepared with molar ratios of 1 SiO₂/0.010 Al₂(SO₄)₃/0.18 NaOH/0.10 C₆₆₆ /40 H₂O. For this, 1.68 g of C₆₆₆, 2.40 g of NaOH (10 wt/wt % Sigma Aldrich, 97 wt% in deionized H₂O), and 13.7 g of deionized H₂O were combined and stirred until homogenized in a PFA jar. Separately, 0.22 g of Al₂(SO₄)₃ · 18H₂O (Sigma-Aldrich, ≥97%) was dissolved in 5 g of deionized H₂O and added dropwise to the first solution. Lastly, 5.01 g of colloidal silica (Ludox AS40, 40 wt/wt %, Sigma-Aldrich) was added to the mixture and stirred for 12 h under ambient conditions. The synthesis solution was then transferred to a 45mL Teflon-lined stainless-steel autoclave in a forced convection oven at 403 K for 7 days under rotation (60rpm).

All synthesized solids were recovered via centrifugation and washed with deionized water until the pH of the supernatant reached a value below 8. To remove the occluded organic content, samples were treated in flowing air at 853 K (0.0167 K s⁻¹) for 10 h (6.9 × 10⁻⁵ mol s⁻¹, UHP, 99.999%, Indiana Oxygen). To obtain the zeolite in NH₄⁺ form, an aqueous ion exchange was performed using a 1.0 M NH₄NO₃ solution (100 cm³ g cat⁻¹, NH₄NO₃ ≥ 98%, Sigma Aldrich, 24 h) followed by washing with deionized H₂O (30 cm³ per g solids, 4×) and dried overnight at 373 K in stagnant air.

SI.2 MFI synthesis using EDA and TPA⁺

The MFI-EDA-8.2 sample used in this study was synthesized using tetrapropylammonium (TPA⁺) and ethylenediamine (EDA) following methodologies outlined by Hur et al.³ and adapted from earlier works by Kester et al.⁴. In the original study, this sample was designated as B-Al-MFI-EDA (B-free,50) where the sample naming convention was B-Al-MFI-EDA (a,b) with ‘a’ representing the Si/B ratio and ‘b’ indicating the Si/Al ratio used in the synthesis gel. The MFI-EDA-8.2 was prepared from a synthesis gel with a molar ratio of 1 SiO₂/0.01Al₂O₃/0.02 TPAOH/0.29EDA/10.2 H₂O. The synthesis procedure started by adding EDA (99.5 wt%, Sigma-Aldrich) to deionized H₂O (18.2 MΩ) in a PFA container and stirring the solution under ambient conditions for 0.25 h. After, aluminum nitrate nonahydrate (Al(NO₃)₃, 90 wt %, Alfa Aesar) and TPAOH (40 wt %, Alfa Aesar) were added to the EDA-containing solution, and the mixture was stirred under ambient conditions for 0.25 h to homogenize the contents. Lastly, colloidal silica (Ludox HS-49, 40 wt %, Sigma Aldrich) was added to the mixture and stirred for 2 h under ambient conditions. The solution was then transferred to a 45mL Teflon-lined stainless-steel autoclave in a forced convection oven at 448 K for 120 h under rotation (50rpm).

The synthesized solid were recovered and washed with deionized H₂O and acetone (Sigma-Aldrich, 99.9 wt %) in alternating steps until the pH of the supernatant remained constant between washes. The solid was then recovered via centrifugation, dried at 373 K under stagnant air for 24 h, and then treated in flowing dry air (1.67 cm³ s⁻¹ g_{cat}⁻¹, 99.999% UHP, Indiana Oxygen) at 853 K (0.0167 K s⁻¹) for 10 h. To obtain the zeolite in NH₄⁻ form, an aqueous ion exchange was performed using 150 cm³ per gram of zeolite of a 1.0 M NH₄NO₃ solution (8.0 wt% in deionized water, 99.9 wt %, Sigma-Aldrich) for 24 h, followed by washing four times with deionized H₂O (70 cm³ per g solids).

SI.3 MFI synthesis using DABCO and MA

MFI samples (MFI-DABCO-3.3 and MFI-DABCO-12.7) were synthesized using a mixture of 1,4-diazabicyclo [2.2.2] octane (DABCO) and methylamine (MA), following the methodologies outlined by Nimlos et al.⁵ In the original publication, these samples were labeled as MFI-DABCO (44,0.04)-2 and MFI-DABCO (44,0.04)-1 using the convention MFI-OSDA (X, Y), where X represents the Si/Al ratio of the solid and Y indicates the Na⁺/OSDA ratio used in the synthesis gel. The gel molar ratio used for the synthesis was SiO₂/0.0125 Al₂O₃/0.36 DABCO/0.36 MA/0.014 Na₂O/13.2 H₂O. The synthesis gel was prepared by adding 3.06 g of DABCO (Sigma-Aldrich, 99%) to a solution of 8.84 g of deionized water (18.2 MΩ) and 2.09 g of CH₃NH₂ (Sigma-Aldrich, 40 wt% in water) and stirred for 30 min. Then 0.08 g of NaOH (Macron, 98%), 0.39 g of aluminum isopropoxide (Sigma-Aldrich, 98%), and 15 g of colloidal silica (Ludox HS-30, Sigma-Aldrich, 30 wt % in water) were added to the solution and stirred at ambient conditions for 4 h. The synthesis gel was then transferred a 45mL Teflon-lined stainless-steel autoclave in a static oven at 413 K for 16 days.

After zeolite crystallization, solids were washed in deionized water and acetone alternating until the pH was constant between washes. The solids were recovered via centrifugation and dried at 373 K for 24 h under stagnant air. Dried solids were treated in flowing air at 853 K for 10 h (1.67 cm³ s⁻¹ g_{cat}⁻¹, 99.999% UHP, Indiana Oxygen) to remove the organic content. To obtain the zeolite in NH₄⁻ form, an aqueous ion exchange was performed using 150 cm³ per gram of zeolite

of a 1.0 M NH_4NO_3 while stirring at ambient conditions for 24 h, followed by washing four times with deionized H_2O and dried at 373 K for 24 h.

SI.4 TON synthesis with varied ISDA/OSDA

TON samples showed in this study were reported in a previous publication.⁶ Zeolites were crystallized using K^+ as an inorganic structure directing agent (ISDA) and 1,8-diaminooctane (DAO) or 1,6-diaminohexane (DAH) as an organic structure directing agent (OSDA). Samples were denoted as TON (X, Y)-Z where X is the Si/Al in the synthesis gel, Y is the K^+ /OSDA ratio in the synthesis gel, and Z indicates the OSDA. KOH was the primary source of hydroxide ions, and all samples were crystallized with ratios of K^+ /OSDA > 0. TON samples with different amount of Al were crystallized from synthesis gel with fixed ISDA/OSDA ratio and varied Al content (Si/Al 30-80). The synthesis gels were prepared with molar ratios of $1\text{SiO}_2/x\text{Al}_2(\text{SO}_4)_3/y\text{KOH}/(0.6-y)\text{OSDA}/31\text{H}_2\text{O}/0.05\text{ seed crystal}$, where x ranged from 0.006 to 0.017 and y ranged from 0.12 to 0.40. A typical synthesis was prepared by combining 1.68 g of KOH (Macron, $\geq 85\%$), 0.38 g of aluminum sulfate octadecahydrate ($\text{Al}_2(\text{SO}_4)_3 \cdot 18\text{H}_2\text{O}$, Sigma-Aldrich, $\geq 97\%$) and 28.78 g of deionized water in a PFA jar and stirred until homogenized. Separately, 3.42 g DAH (Aldrich, 98 %) and 14.39 g of deionized water was combined and stirred until homogenized. The contents of the 2 PFA jars were combined, and 20.00 g of colloidal silica (LUDOX, AS-30) were added to the mixture and stirred for ~ 2 h. The gel mixture was separated into 45 mL Teflon-lined stainless-steel autoclaves and 0.15 g of a commercially sourced TON sample (ACS Material, MSZ22H12) was added to each liner as seed crystal and stirred with a spatula. After, autoclaves were sealed, aged 24 h at ambient temperature, and then placed in a forced convection oven at 433 K for 48 h under rotation. The same procedure was performed to prepare TON samples with 1,8-diaminooctane (Sigma Aldrich, 98%) as an OSDA.

Crystallized solids were recovered via centrifugation, washed with $3\times$ deionized water ($30\text{ cm}^3\text{ g}^{-1}$), $3\times$ with acetone/water mixture (50% w/w) and $1\times$ with deionized water, or until the pH of the supernatant reached a value before 8. To remove the organic content, solids were treated in flowing air while heating to 648 K (0.0167 K s^{-1}) and holding isothermally for 10 h and subsequently heating to 853 K (0.0167 K s^{-1}) and holding isothermally for 10 h ($6.9 \times 10^{-5}\text{ mol s}^{-1}$, UHP, 99.999%, Indiana Oxygen).

S2. Characterization of Zeolites

S2.1 X-Ray Diffraction Patterns on MFI and TON zeolites

X-ray diffraction (XRD) was used to determine the topology of crystallized MFI and TON samples. XRD patterns were collected on a Rigaku SmartLab X-ray diffractometer with a Cu K α radiation sourced operated at 1.76 kW (40 kV, 44 mA). Samples were measured using diffraction patterns from 4-40° at a step size of 0.01° and scan rate of 0.0167° s⁻¹.

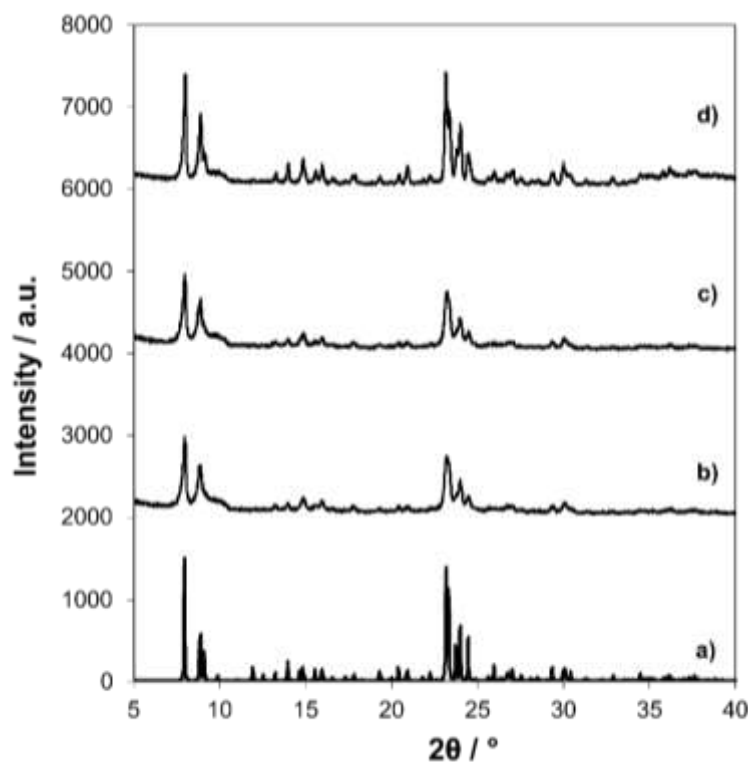


Figure S1. a) MFI XRD pattern from Treacy and Higgings⁷ b) MFI- C₆₆₆-0.03, c) MFI-TPA-0.06, d) MFI-TPA-0.33. Figure reproduced from Bickel et al.¹ Copyright 2023 American Chemical Society.

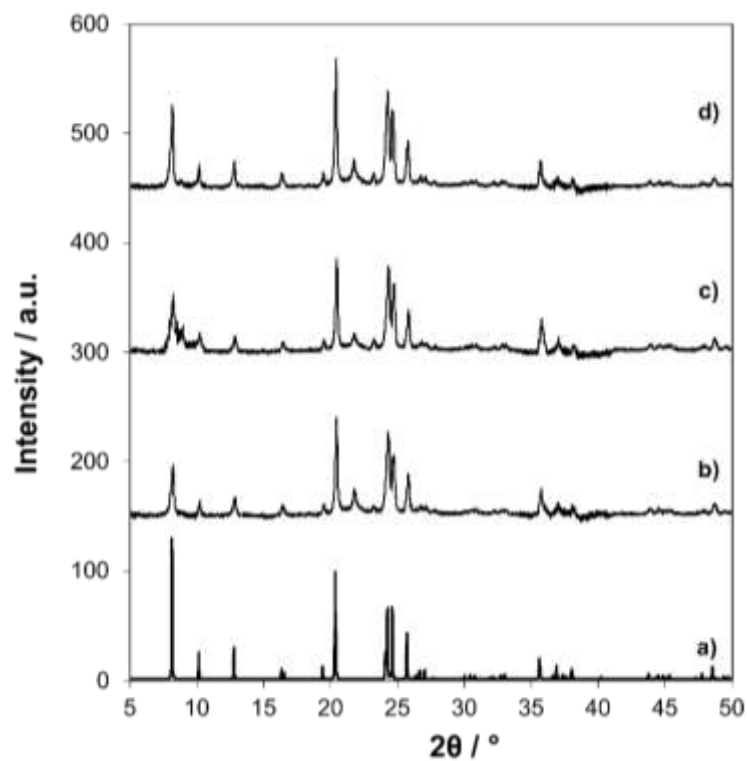


Figure S2. a) TON XRD pattern reproduced by Treacy and Higgins⁷, and measured for TON zeolites with Si/Al \sim 45 that were synthesized with varied ratios of K^+ /DAO b) TON(45, 0.5)-O, c) TON (45, 1.0)-O, d) TON(45.1.5)-O. Figure reproduced with permission from Bickel et al.⁶ Copyright 2023 Elsevier.

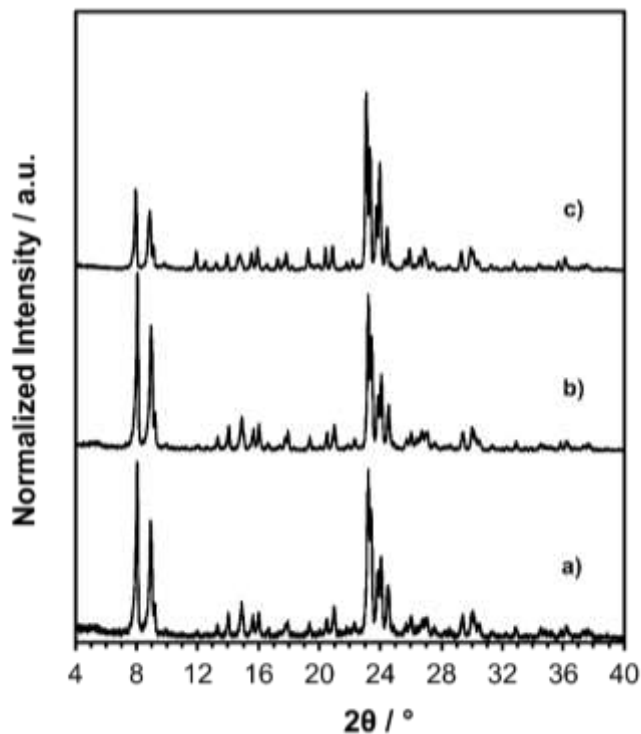


Figure S3. XRD patterns of MFI samples with Si/Al \sim 50 a) MFI-EDA-8.2, b) MFI-DABCO-12.7, c) MFI-DABCO-3.3 reproduced from Ezenwa et al.⁸ Copyright 2024 American Chemical Society.

S2.2 N₂ Adsorption Isotherms on MFI and TON zeolites

Micropore volumes were determined from N₂ adsorption isotherms at 77 K using a Micromeritics 3-flex Adsorption Analyzer. MFI and TON zeolites were degassed at 393 K under vacuum, held isothermally for 2 h, heated to 623 K under vacuum, and held again isothermally for 9 h. Micropore volumes were estimated by the extrapolation of liquid N₂ ($P/P_0 = 0.05$ - 0.90 , 77 K) on degassed samples to zero pressure. Measurements were also consistent with micropore volumes estimated from the minimum of the semilogarithmic derivative plot of the isotherm $\partial(V_{ads})/\partial(\ln(P/P_0))$ which correspond to the pressure where the micropores have been filled.

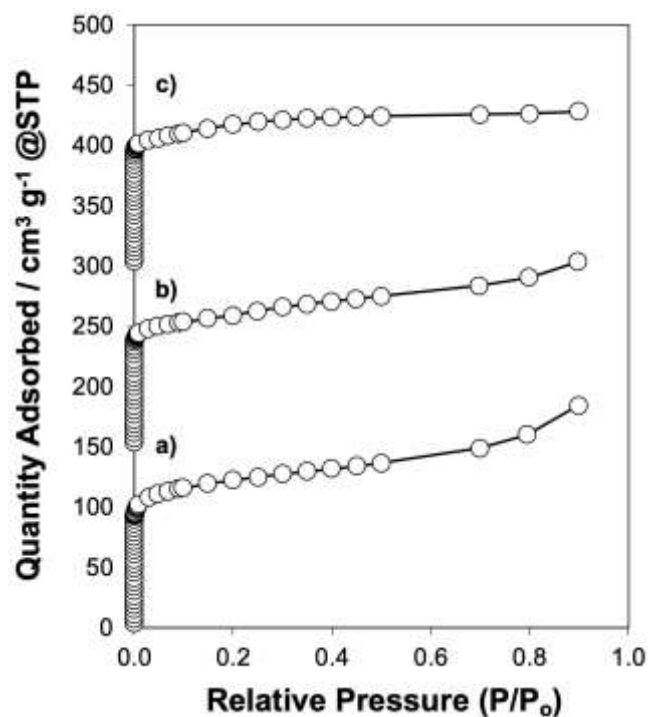


Figure S4. N₂ adsorption-desorption isotherms (77 K) for MFI samples with Si/Al ~50 a) MFI-C₆₆₆-0.03, c) MFI-TPA-0.06, d) MFI-TPA-0.33. Isotherms vertically offset by 150 cm³ g⁻¹ for clarity. Figure reproduced from Bickel et al.¹ Copyright 2023 American Chemical Society.

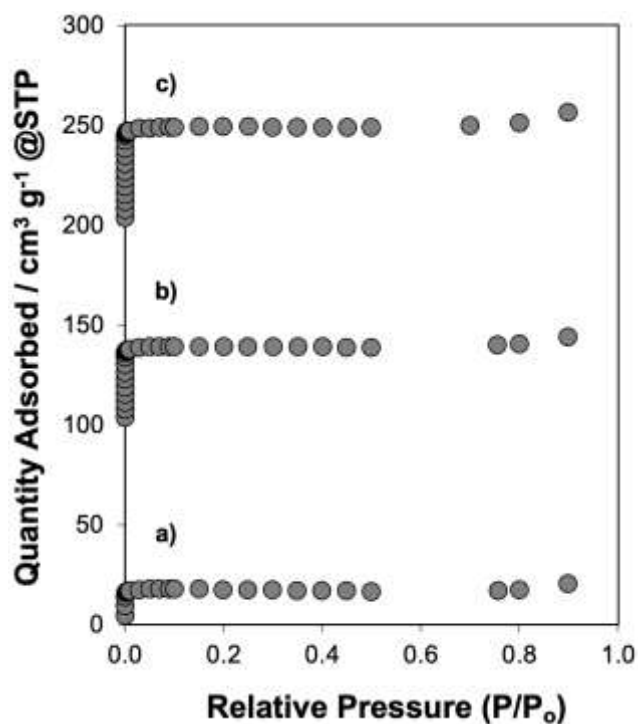


Figure S5. N₂ adsorption-desorption isotherms (77 K) for TON samples with Si/Al ~45 that were synthesized with varied ratios of K⁺/DAO b) TON(45, 0.5)-O, c) TON (45, 1.0)-O, d)

TON(45.1.5)-O. Isotherms vertically offset by $100 \text{ cm}^3 \text{ g}^{-1}$ for clarity. Figure reproduced with permission from Bickel et al.⁶ Copyright 2023 Elsevier.

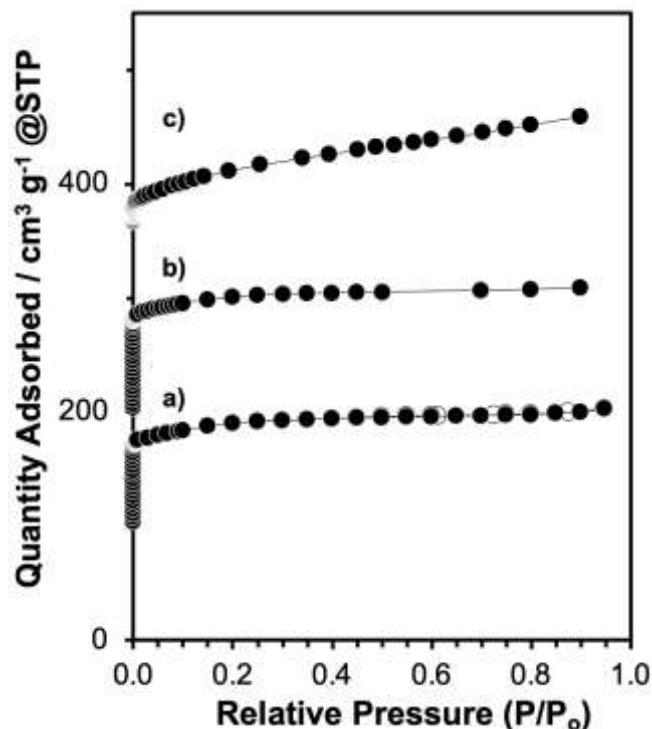


Figure S6. N_2 adsorption-desorption isotherms (77 K) for MFI zeolites with Si/Al ~ 50 a) MFI-EDA-8.2, b) MFI-DABCO-12.7, c) MFI-DABCO-3.3. Isotherms are vertically offset for clarity. Figure adapted from Ezenwa et al.⁸ Copyright 2024 American Chemical Society.

S2.3 Temperature Programmed Desorption Profiles for NH_4 -Form Zeolite Samples

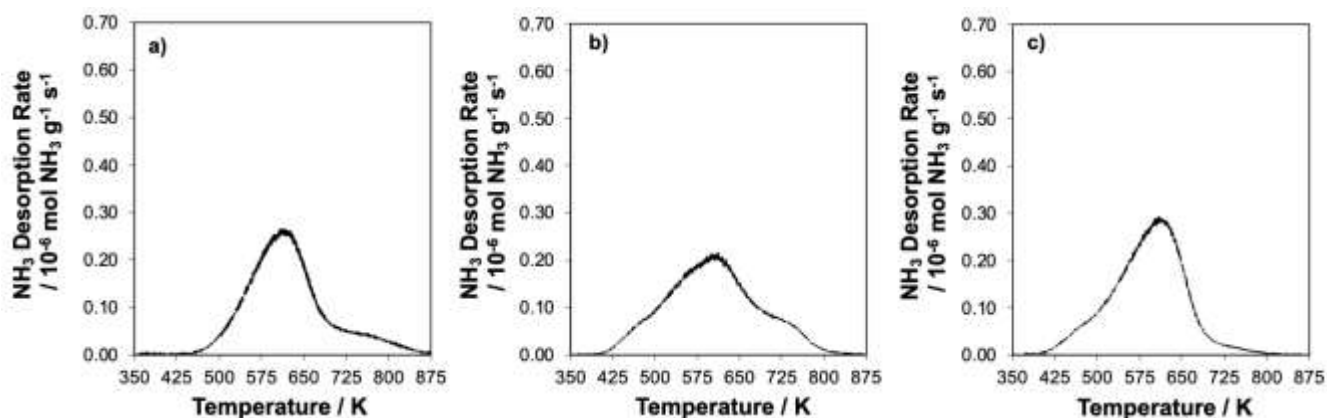


Figure S7. NH_3 TPD profiles for NH_4 -form MFI samples with Si/Al ~ 50 a) MFI- C_{666} -0.03, b) MFI-TPA-0.06, c) MFI-TPA-0.33. Figure reproduced from Bickel et al.¹ Copyright 2023 American Chemical Society.

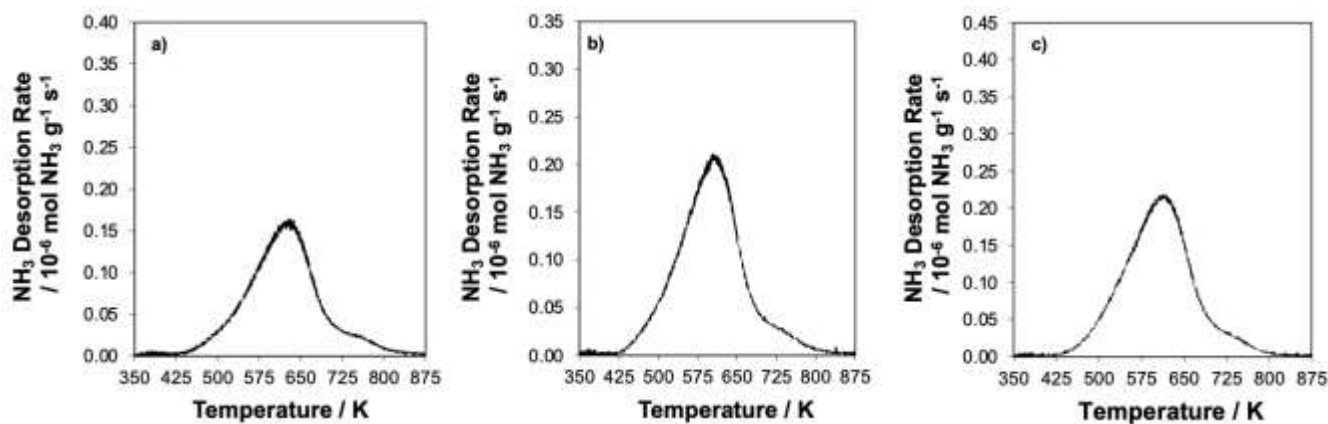


Figure S8. NH₃ TPD profiles for NH₄-form TON samples with Si/Al ~ 45 that were synthesized with varied ratios of K⁺/DAO a) TON(45, 0.5)-O, b) TON (45, 1.0)-O, c) TON(45.1.5)-O. Figure reproduced with permission from Bickel et al.⁶ Copyright 2023 Elsevier.

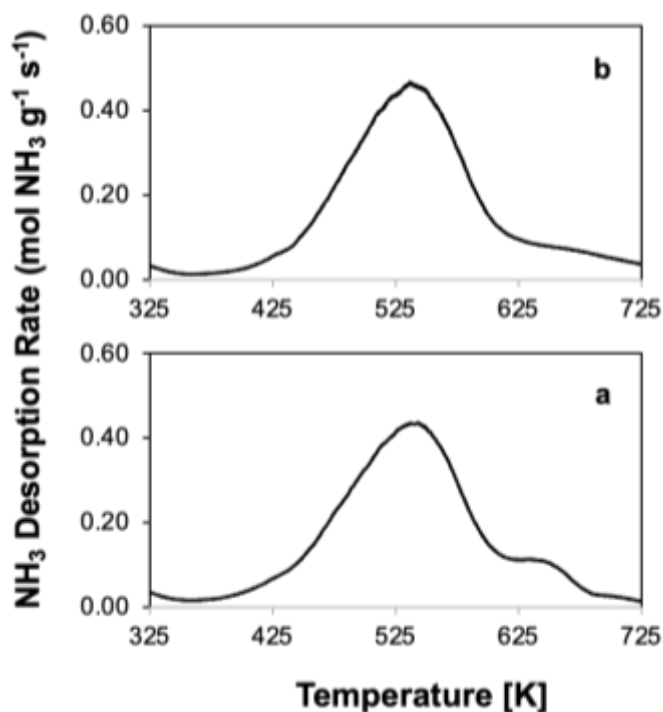


Figure S9. NH₃ TPD profiles for NH₄-form TON samples with Si/Al ~ 50 a) MFI-DABCO-3.3 b) MFI-DABCO-12.7. Figure reproduced from Nimlos et al.⁵ Copyright 2020 American Chemical Society.

S2.4 Elemental Composition and Cobalt Titration

Elemental composition using an inductively coupled plasma optical emission spectrometry (ICP-OES) with a Thermo Scientific iCAP 7000 Plus Series ICP-OES was performed to calculate the total Si, Al, and Co for synthesized samples in H⁺-form and Co-form. Samples in Co-form were obtained by liquid phase ion exchange using 0.5 M Co (NO₃)₂ solution using 150 cm³ of solution per gram of zeolite at 353 K for 24 h. Moreover, Co-form zeolites were wash 6 times with deionized water, dried at 373 K and treated in air to 773 K for 4 h. Samples were prepared by digesting 0.01-0.02 g of MFI and TON zeolites in 2.0-3.0 g of hydrofluoric acid solution (48 wt%) for 24 h following by the addition of 45-55 g of deionized water and approximately 1 g of nitric acid (40 wt%). Elemental composition was determined using standards of known concentration to perform calibration curves.

Ammonia temperature programmed desorption (NH₃ TPD) using a Micrometrics AutoChem II 2920 Chemisorption Analyzer and an Agilent 5973N mass selective detector (MSD) was used to quantify the number of H⁺-sites for synthesized MFI and TON samples in H⁺-form and Co-form. Synthesized samples in ammonium (NH₄) and cobalt (Co) form (0.02g -0.04g) were supported between two quartz wool plugs in a quartz reactor. H⁺-sites quantification on NH₄-form was achieved by flowing He at ambient temperature for 1 h and heated to 873 K (0.167 K s⁻¹). The effluent stream from the quartz cell was sent via heated transfer lines held at 383 K to the MSD for analysis. To quantify residual H⁺-sites on Co-form, samples were exposed to an oxidative treatment (dry air at 0.833 cm³ s⁻¹, to 673 K for 2 h, 0.167 K s⁻¹), after which NH₃ titration of H⁺ sites was performed using a gas-phase titration method. This by flowing a stream of 500 ppm NH₃ in balance He at 433 K for 4 h follow by a stream of wet He (~ 3% H₂O) at 433 K for 8 h to desorb NH₃ bound at non-protonic sites. Argon (Ar) pulses were used to determine a response factor (NH₃/Ar) and an Ar pulse introduced after each NH₃ TPD was used to quantify the amount of NH₃ evolved during the experiment.

Table S1. Characterization data from Elemental Composition and NH₃ TPD.

Sample ^a	Si/Al _{tot} ^b (solid)	H ⁺ /Al _{tot} ^c	Co ²⁺ /Al ^d
MFI-DABCO-3.3	44	0.95	0.06
MFI-DABCO-12.7	44	0.85	0.14
MFI-EDA-8.2	58	0.92	0.01
MFI-C ₆₆₆ -0.03	47	0.81	0.38
MFI-TPA-0.06	54	0.80	0.40
MFI-TPA-0.33	55	0.84	0.11

^aSample nomenclature is MFI-X-Y; X indicates the major OSDA, and Y denotes the crystallite size by SEM.

^bDetermined by ICP-OES. Uncertainty is ± 10%.

^cDetermined from liquid-phase NH₄ ion exchange followed by NH₃ TPD. Uncertainty is ± 10%.

^dFraction of proximal anionic Al measured using reported cobalt divalent ion (Co²⁺) titration techniques³.

S2.5 Scanning Electron Microscopy (SEM) images for MFI and TON samples

The quantification of crystallite size was achieved using Scanning Electron Microscopy (SEM) on a FEI Quanta 3D FEG Dual-beam SEM instrument equipped with an Everhart-Thornley

detector for high vacuum imaging (2-7 kV) and a spot size range of 1-5 μm . The mean crystallite size was taken to be the average length of the shortest dimension of the crystallite estimated for ≥ 30 crystallites. SEM mean crystallite sizes and standard deviations are summarized in Table 1. The sampling number was increased from ~ 45 crystals (Fig. SX) to ~ 280 crystals (Fig. SX) for a representative sample, MFI-DABCO-3.3, to ensure the sample size was large enough, and the mean crystallite size did not change with sample size ($3.3 \pm 0.6 \mu\text{m}$ for ~ 45 crystals versus $3.2 \pm 0.6 \mu\text{m}$ for ~ 280 crystals).

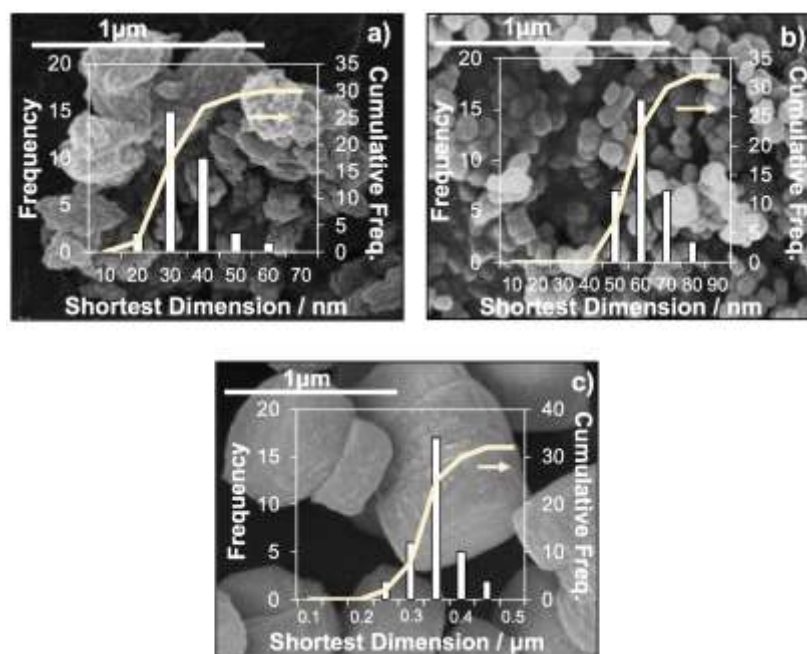


Figure S10. Representative SEM images and crystallite size distributions for MFI samples with Si/Al ~ 50 a) MFI- C₆₆₆-0.03, c) MFI-TPA-0.06, d) MFI-TPA-0.33. Figure reproduced from Bickel et al.¹ 2023 American Chemical Society.

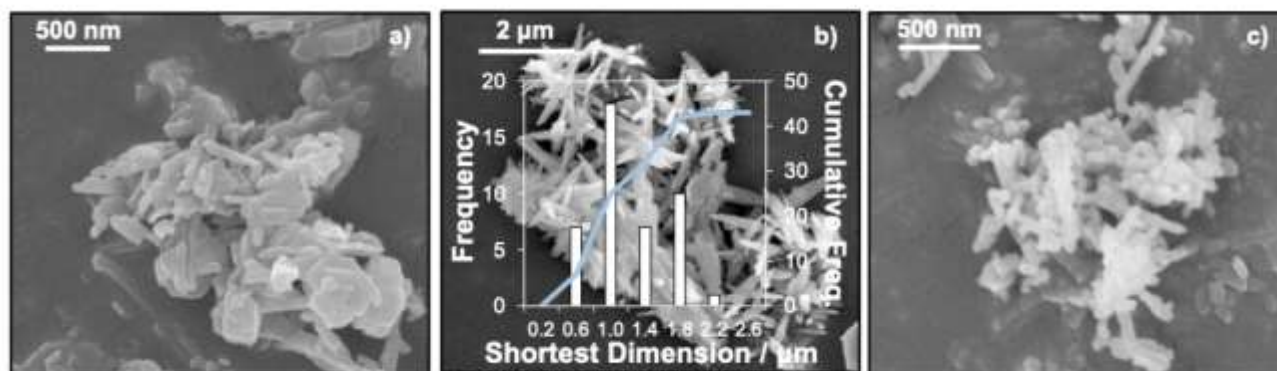


Figure S11. Representative SEM images and crystallite size distributions for TON samples with Si/Al ~ 45 that were synthesized with varied ratios of K^+/DAO b) TON(45, 0.5)-O, c) TON (45,

1.0)-O, d) TON(45.1.5)-O. Figure reproduced with permission from Bickel et al.⁶ Copyright 2023 Elsevier.

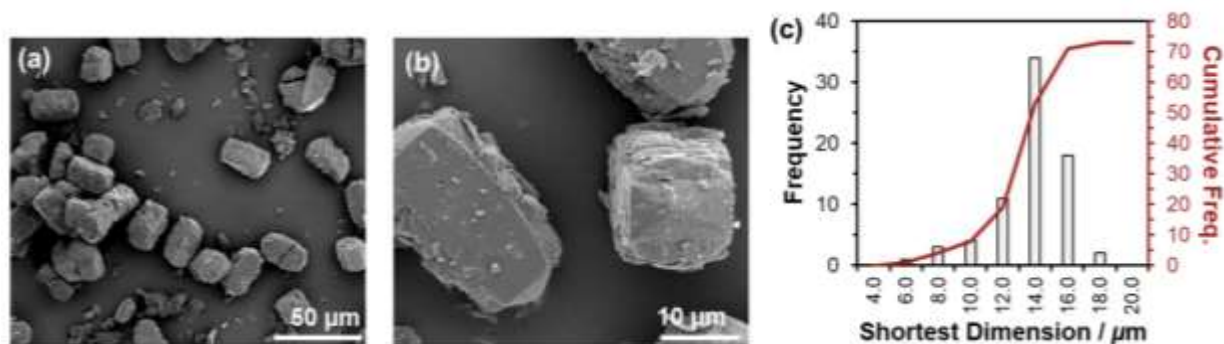


Figure S12. Representative SEM images (a-b) and crystallite size distributions (c) for MFI-DABCO-12.7. Figure reproduced from Ezenwa et al.⁸ Copyright 2024 American Chemical Society.

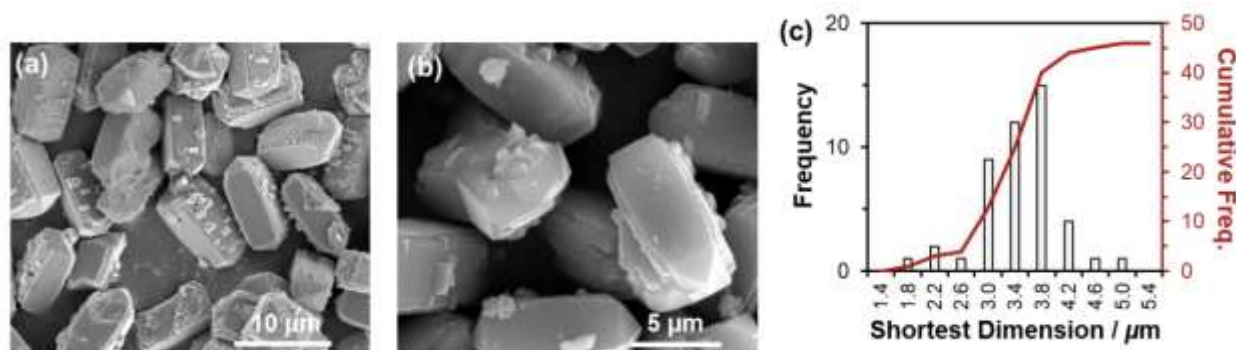


Figure S13. Representative SEM images (a-b) and crystallite size distributions (c) for MFI-DABCO-3.3. Figure reproduced from Ezenwa et al.⁸ Copyright 2024 American Chemical Society.

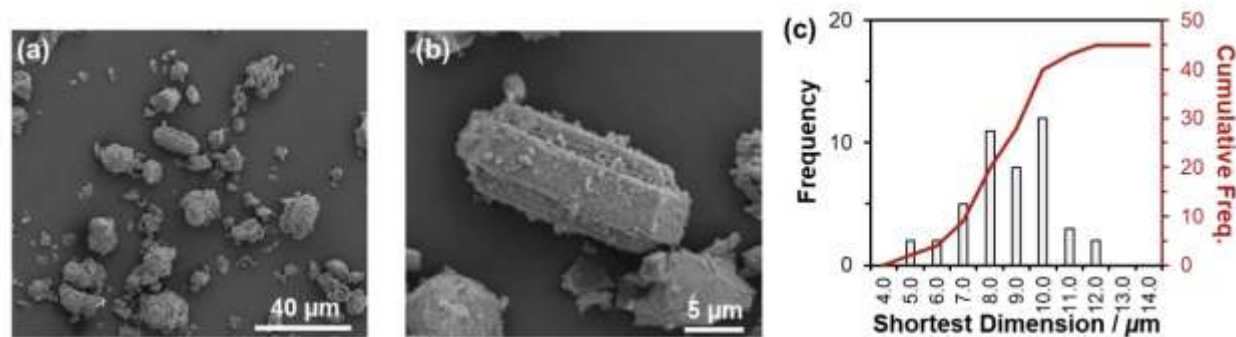


Figure S14. Representative SEM images (a-b) and crystallite size distributions (c) for MFI-EDA-8.2. Figure reproduced from Ezenwa et al.⁸ Copyright 2024 American Chemical Society.

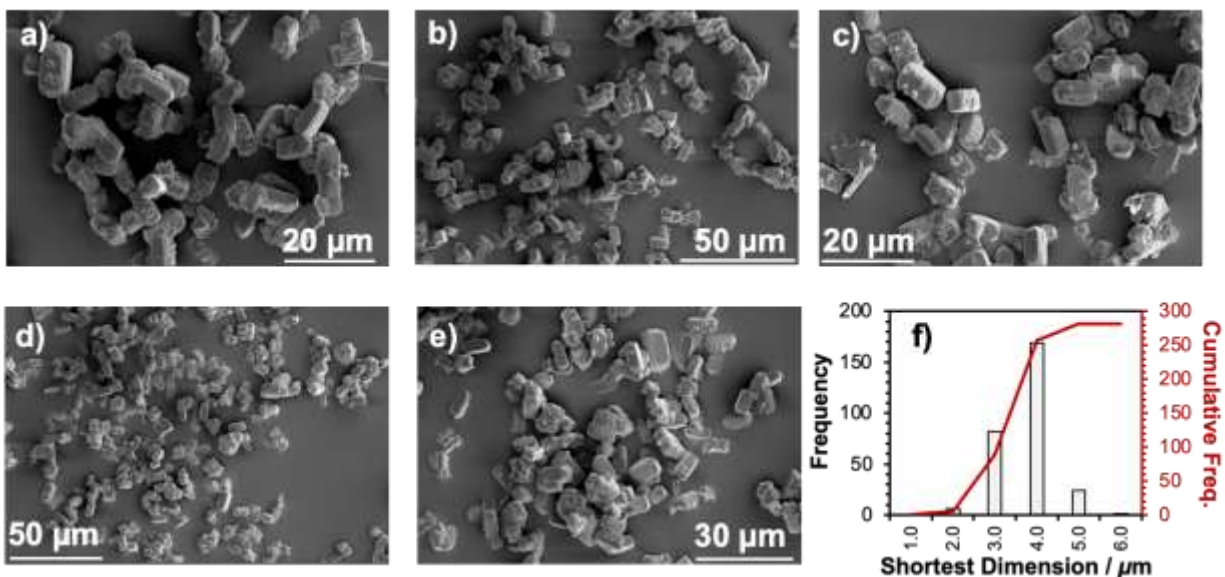


Figure S15. Representative SEM images (a-e) and crystallite size distributions (f) for MFI-DABCO-3.2 sampling 282 crystals.

S3. Propene Oligomerization Kinetic Measurements

Propene oligomerization reactions were performed using a stainless-steel reactor (9.5 mm i.d.) This reactor has a concentric thermowell (stainless steel 1/8 in. diameter) with a K-type thermocouple extended through the axial center of the reactor into the center of the catalyst bed to record bed temperature over the course of the experiments. NH₄-MFI zeolites were loaded into the reactor supported by quartz wool and two stainless steel rods on both sides. Silica (60-100 mesh) was used to dilute the catalyst performing a physical dilution. In this physical dilution, zeolite samples were pelletized and sieved to retain 180-250 μm particles follow by the mixing with silica (0.05 ratio catalyst-silica weight ratio) to obtain a total bed mass of $\sim 0.5\text{g}$.

Before reaction, the sample was pretreated ($1.7 \times 10^{-5} \text{ mol s}^{-1}$ flowing air and $5.1 \times 10^{-5} \text{ mol s}^{-1}$ flowing Ar) to remove physisorbed water and to convert samples to H-form. The temperature was ramped at 1.5 K min^{-1} until 823 K, held for 5 hours and then ramped down to reaction temperature. After the pretreatment, the reactor was purged with argon for at least 1.5 hours before starting the reactions. Reactant flows were composed of 95 mol % propene and 5 mol% methane (internal standard) and the pressure upstream of the catalyst bed was controlled by a back pressure regulator located downstream. Products were measured using methane as an internal standard with injections starting after 10 min time on stream. Species exiting the reactor were quantified using a gas chromatograph (Agilent 7890 A) equipped with a flame ionization detector (GS GasPro column, 0.320 mm i.d. x 60 m x 10 μm , Agilent).

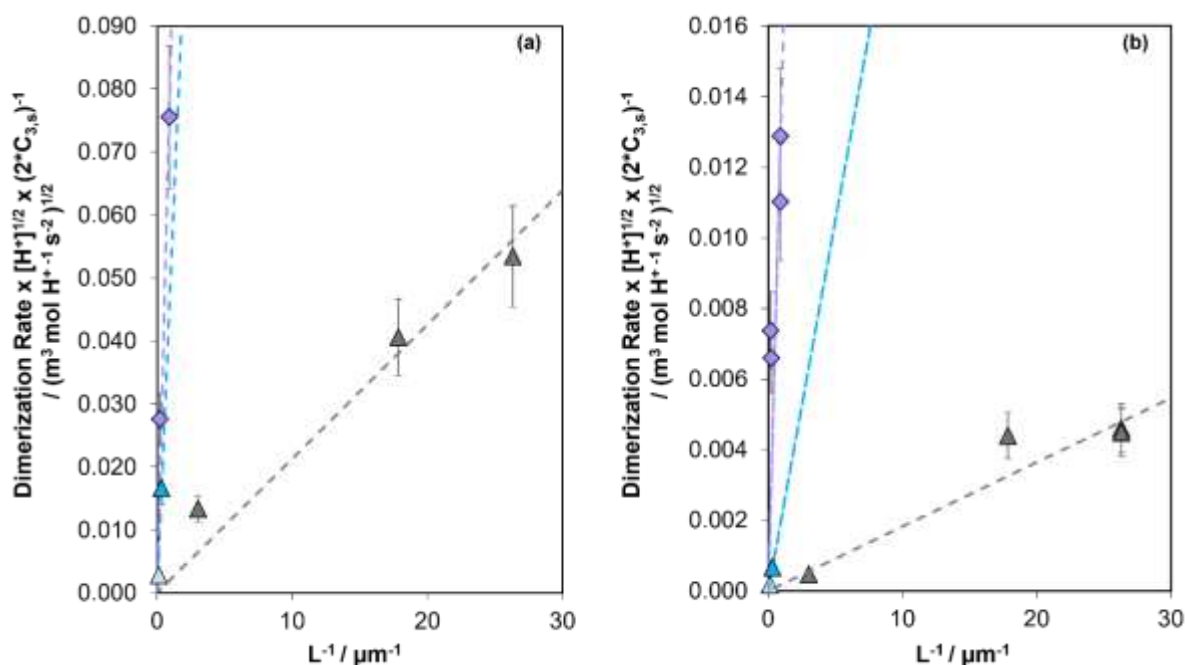


Figure S16. Dimerization rates times the H⁺-site density ($[\text{H}_0^+]$) as function of the inverse of crystallite size at **a)** 16 kPa C₃H₆ and **b)** 605 kPa C₃H₆ for MFI-DABCO (dark blue) and MFI-EDA (light blue) used in this study and for MFI-TPA (gray) reproduced from Bickel et al.¹ (copyright 2023 American Chemical Society) and for TON (purple) reproduced with permission from Bickel et al.⁶ (copyright 2023 Elsevier).

S4. MFI Framework Details

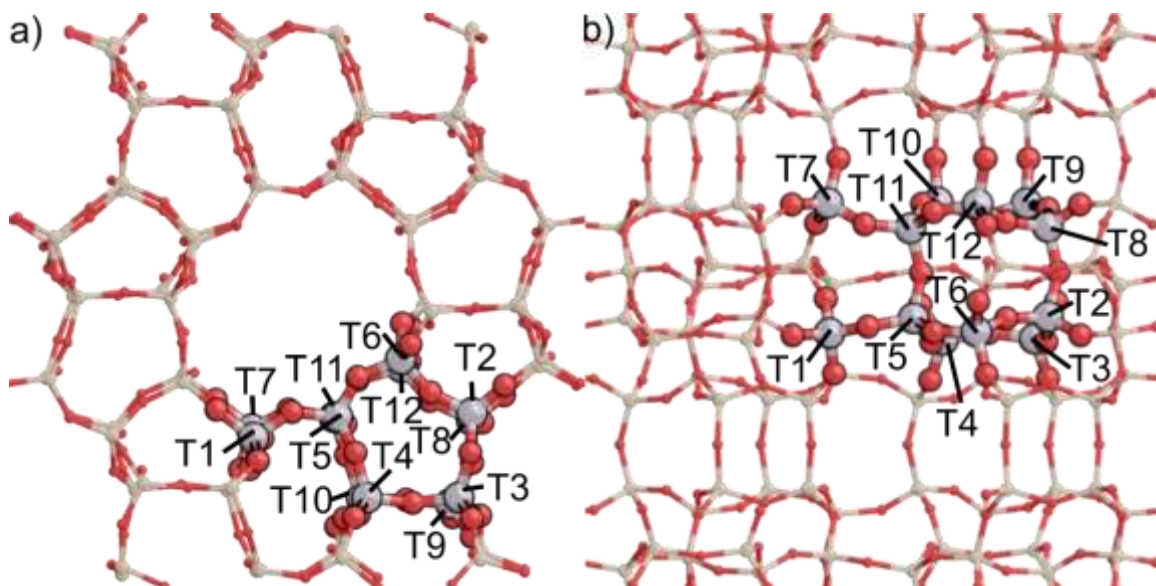


Figure S17. MFI framework from the a) 010 and b) 001 views with each of the 12 crystallographically unique T-sites labeled.

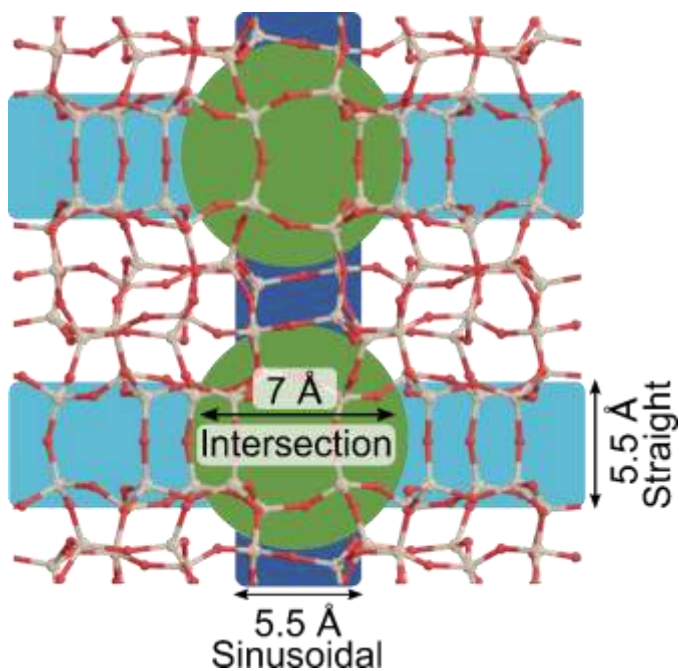


Figure S18. MFI framework from the 001 view with the void environments shaded by color (green for intersection, light blue for straight channel, and dark blue for sinusoidal channel) along with the corresponding diameter for each environment.

S5. MFI O-atom Indices and Classification

Table S2. O-atom indices used in this text, the corresponding indices from van Koningsveld et al. (from which the structure used in this work was constructed), the corresponding void environment in which each O-site resides, and the T-sites associated with each O-site. O-sites located in a subunit (O4, O20, and O24) are considered inaccessible and were not included in this study.

This work ^a	O-site	Void Environment	T-sites bound to O-site	
	van Koningsveld et al. ^b			
O1	O21	Int	T1	T5
O2	O1	Int	T1	T2
O3	O15	Int	T1	T10
O4	O16	Subunit	T1	T4
O5	O2	Int	T2	T3
O6	O13	Str	T2	T8
O7	O6	Sin	T2	T6
O8	O20	Int	T3	T12
O9	O3	Sin	T3	T4
O10	O19	Str	T3	T6
O11	O17	Sin	T4	T7
O12	O4	Sin	T4	T5
O13	O5	Int	T5	T6
O14	O14	Str	T5	T11
O15	O18	Int	T6	T9
O16	O22	Int	T7	T11
O17	O7	Int	T7	T8
O18	O23	Int	T7	T7
O19	O8	Int	T8	T9
O20	O12	Subunit	T8	T12
O21	O25	Int	T9	T9
O22	O9	Sin	T9	T10
O23	O26	Int	T10	T10
O24	O10	Subunit	T10	T11
O25	O11	Int	T11	T12
O26	O24	Int	T12	T12

^aFrom the International Zeolite Association numbering for the MFI framework.⁹

^bFrom van Koningsveld et al.¹⁰

S6. Temperature-Corrected Entropy and Enthalpy Calculations

Temperature-corrected free energies (G) and enthalpies (H) were calculated for all optimized and Dimer structures. Normal mode analysis frequency calculations were used to calculate zero-point vibrational energies (ZPVE), vibrational enthalpy (H_{vib}), and vibrational entropies (S_{vib}) to determine the enthalpy for adsorbed states:

$$H = E_0 + ZPVE + H_{vib} \quad (S1)$$

and Gibbs free energy:

$$G = E_0 + ZPVE + G_{vib} \quad (S2)$$

For gas phase propene, the rotational enthalpy (H_{rot}), translational enthalpy (H_{trans}), rotational free energy (G_{rot}), and translational free energy (G_{trans}) were also calculated to determine the enthalpy:

$$H = E_0 + ZPVE + H_{vib} + H_{rot} + H_{trans} \quad (S3)$$

and Gibbs free energy:

$$G = E_0 + ZPVE + G_{vib} + G_{rot} + G_{trans} \quad (S4)$$

All temperature-corrected calculations were performed at 503 K.

S7. Deprotonation Energies (DPE) per O-site

Table S3. Deprotonation energies at each O-site in MFI sorted based on O-site void environment.

T-site	O-site	Void Environment	DPE <i>kJ mol⁻¹</i>	Average DPE per Environment
T2	O7	sin	1657	1651
T6	O7	sin	1651	
T3	O9	sin	1654	
T4	O9	sin	1638	
T4	O11	sin	1657	
T7	O11	sin	1657	
T4	O12	sin	1648	
T5	O12	sin	1649	
T9	O22	sin	1649	
T10	O22	sin	1647	
T2	O6	straight	1660	1655
T8	O6	straight	1653	
T3	O10	straight	1665	
T6	O10	straight	1660	
T5	O14	straight	1649	
T11	O14	straight	1643	
T1	O1	int	1648	1649

T5	O1	int	1646	
T1	O2	int	1643	
T2	O2	int	1644	
T1	O3	int	1651	
T10	O3	int	1649	
T2	O5	int	1652	
T3	O5	int	1649	
T3	O8	int	1649	
T12	O8	int	1644	
T5	O13	int	1654	
T6	O13	int	1655	
T6	O15	int	1647	
T9	O15	int	1648	
T7	O16	int	1645	
T11	O16	int	1640	
T7	O17	int	1665	
T8	O17	int	1661	
T7	O18	int	1652	
T8	O19	int	1653	
T9	O19	int	1654	
T9	O21	int	1647	
T10	O23	int	1647	
T11	O25	int	1645	
T12	O25	int	1645	
T12	O26	int	1638	
<hr/>				
T1	O4	subunit	1648	1650
T4	O4	subunit	1645	
T8	O20	subunit	1642	
T12	O20	subunit	1643	
T10	O24	subunit	1663	
T11	O24	subunit	1658	
<hr/>				

S8. Adsorption Free Energy of C3 species at Each O-site

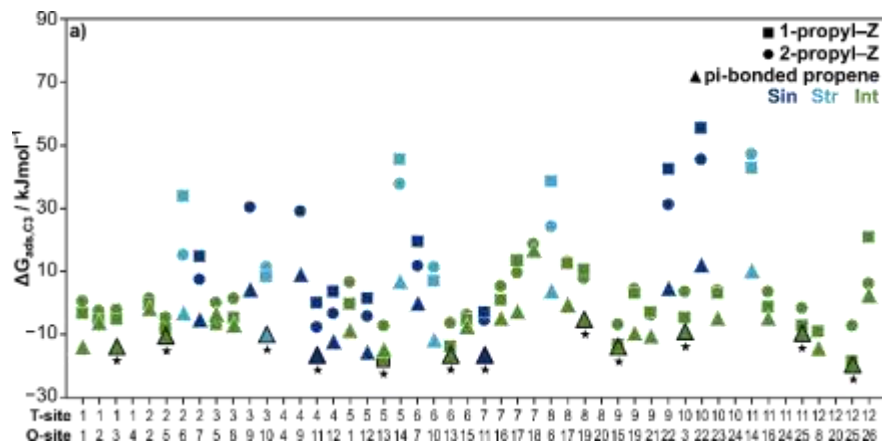


Figure S19. Adsorption free energies ($\Delta G_{\text{ads},C3}$ kJ mol^{-1}) for 1-propyl-Z (circles), 2-propyl-Z (squares), and H-bonded propene (triangles) in the sinusoidal channel (dark blue), straight channel (light blue), and intersection (green) at 503 K. Data points with a black star correspond to the C₃ species with the lowest $\Delta G_{\text{ads},C3}$ per T-site (the same data presented in Figure 5c). Figure 5a in the main text is a reorganized version of this figure organized by void environment instead of O-site.

S9. Adsorption Free Energy of Most Stable C₃ Adsorbate at Each O-site

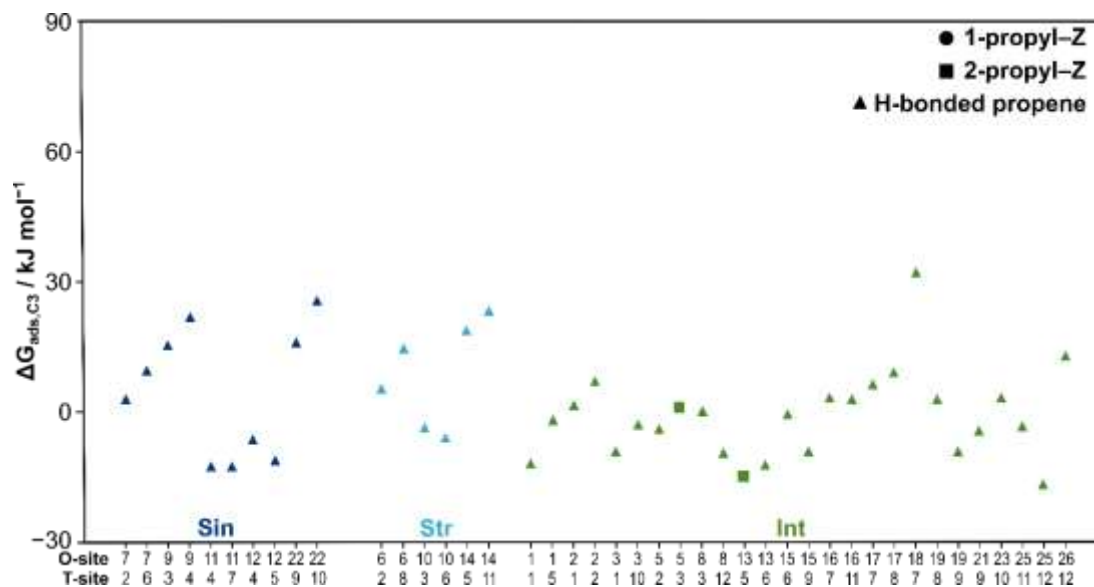


Figure S20. The lowest $\Delta G_{\text{ads,C3}}$ of all C₃ adsorbates, 1-propyl-Z (circles), 2-propyl-Z (squares), and H-bonded propene (triangles), per O-site at 503 K. O-sites are organized based on void environment: sinusoidal channel is dark blue, straight channel is light blue, and intersection is green.

S10. Binding Free Energy of C₃ Adsorbates at Each T-site

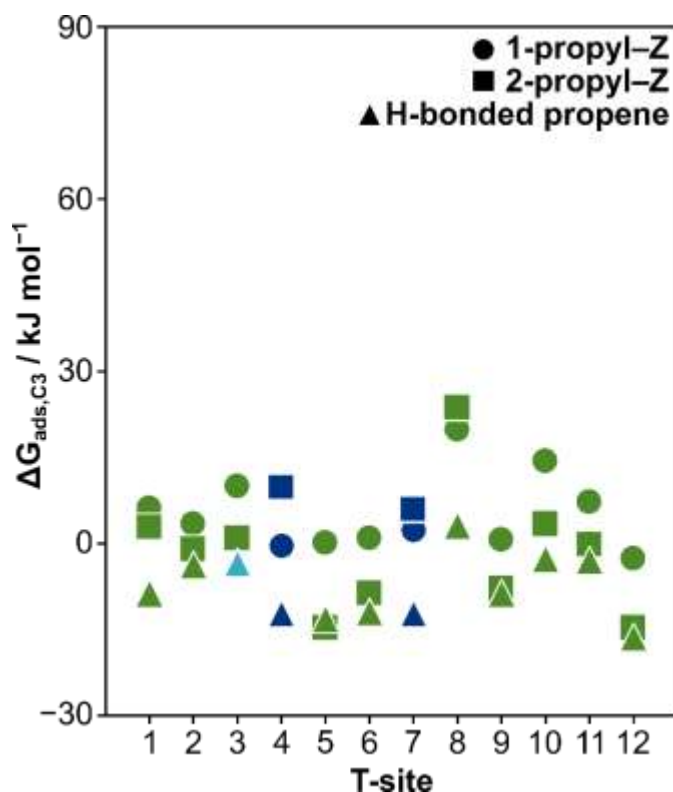


Figure S21. The lowest $\Delta G_{\text{ads,C3}}$ for each species (1-propyl-Z (circles), 2-propyl-Z (squares), and H-bonded propene (triangles)) per T-site at 503 K. The environment of the corresponding O-site is indicated with color: sinusoidal channel is dark blue, straight channel is light blue, and intersection is green.

S11. Images of C₃ Adsorbates at Each T-site

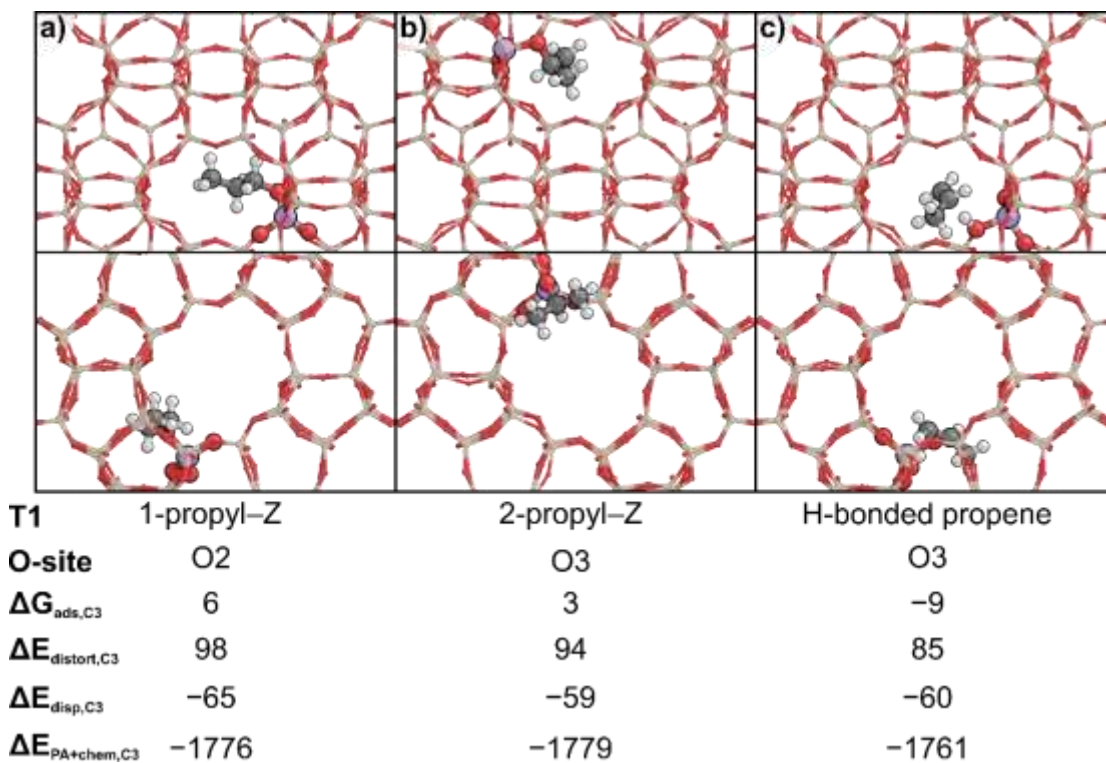


Figure S22. **a)** 1-propyl-Z, **b)** 2-propyl-Z, **c)** and H-bonded propene structures with the lowest ΔG_{Ads} at T1 viewed through the sinusoidal (top) and straight (bottom) channels. $\Delta G_{\text{ads,C3}}$ values are reported at 503 K. $\Delta E_{\text{distort,C3}}$, $\Delta E_{\text{disp,C3}}$, and $\Delta E_{\text{PA+chem,C3}}$ are calculated according to Eqs. 13, 14 and 15, respectively, in the main text.

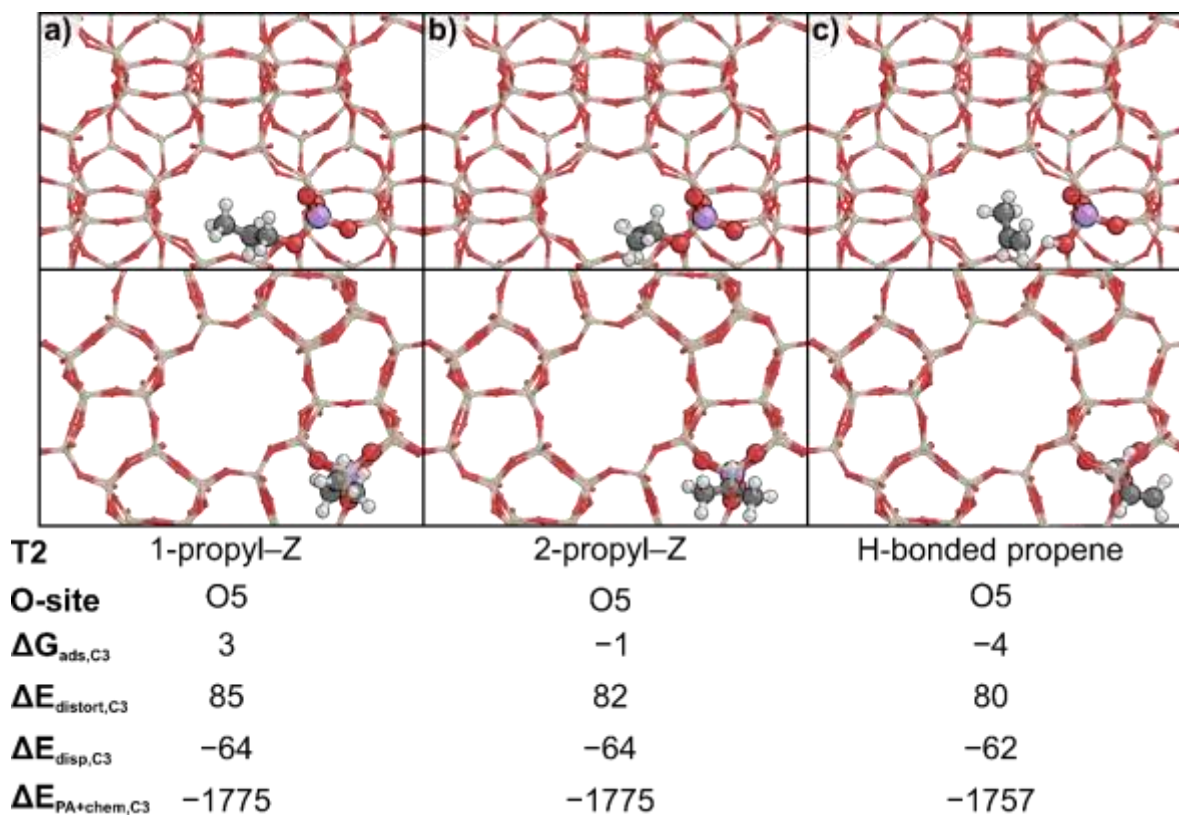


Figure S23. a) 1-propyl-Z, b) 2-propyl-Z, c) and H-bonded propene structures with the lowest ΔG_{Ads} at T2 viewed through the sinusoidal (top) and straight (bottom) channels. $\Delta G_{\text{ads,C3}}$ values are reported at 503 K. $\Delta E_{\text{distort,C3}}$, $\Delta E_{\text{disp,C3}}$, and $\Delta E_{\text{PA+chem,C3}}$ are calculated according to Eqs. 13, 14 and 15, respectively, in the main text.

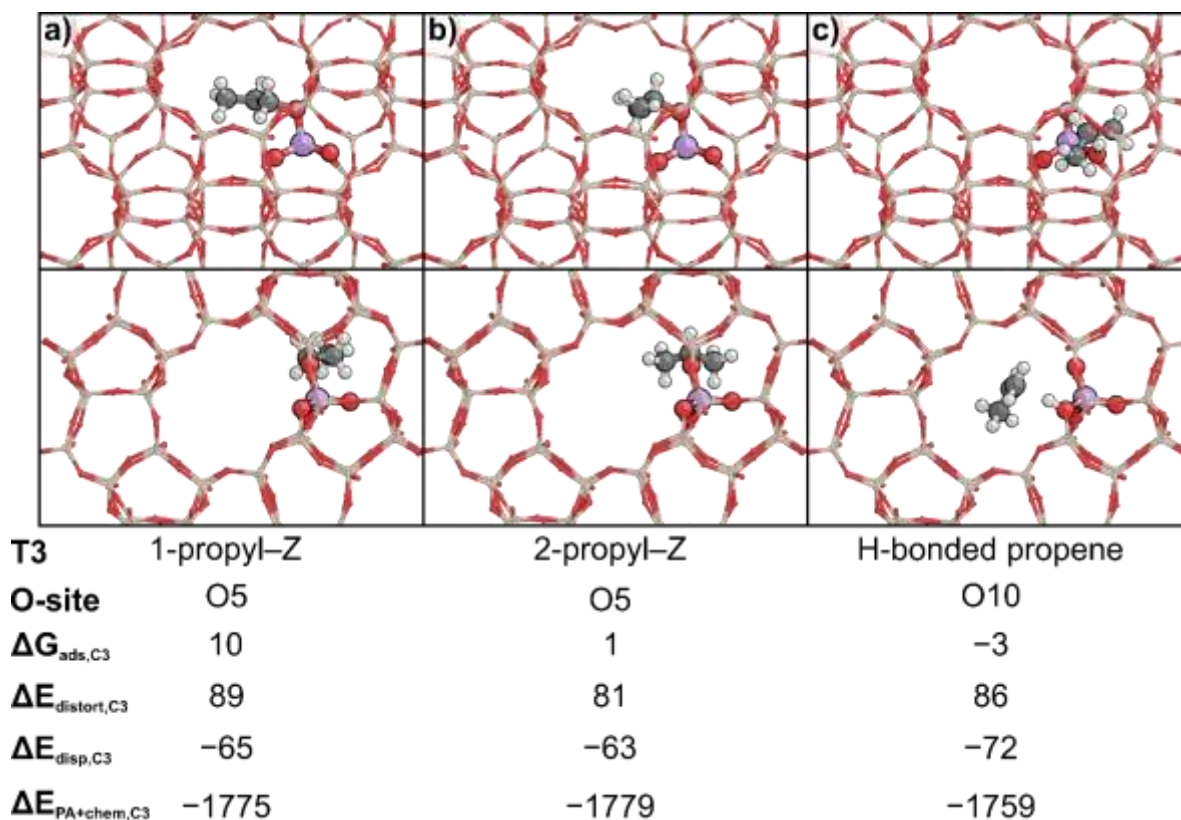


Figure S24. **a)** 1-propyl-Z, **b)** 2-propyl-Z, **c)** and H-bonded propene structures with the lowest ΔG_{Ads} at T3 viewed through the sinusoidal (top) and straight (bottom) channels. $\Delta G_{\text{ads,C3}}$ values are reported at 503 K. $\Delta E_{\text{distort,C3}}$, $\Delta E_{\text{disp,C3}}$, and $\Delta E_{\text{PA+chem,C3}}$ are calculated according to Eqs. 13, 14 and 15, respectively, in the main text.

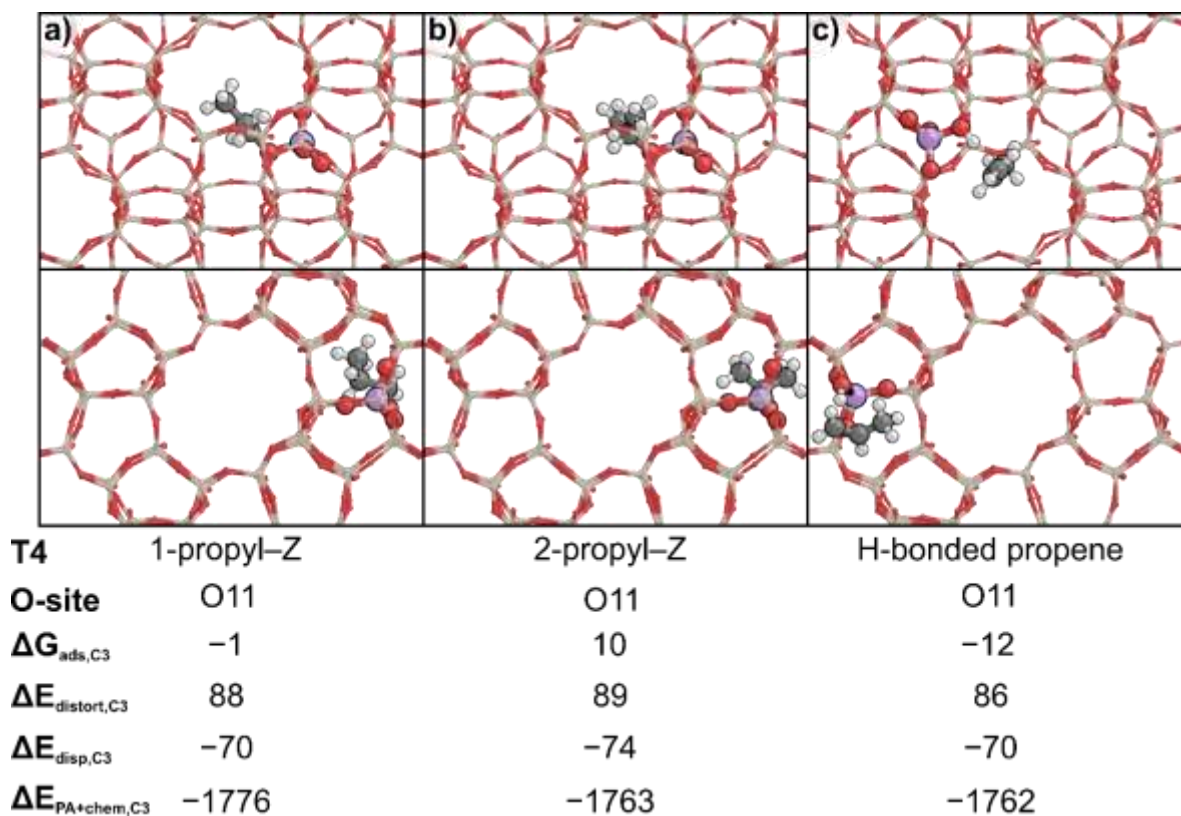


Figure S25. **a)** 1-propyl-Z, **b)** 2-propyl-Z, **c)** and H-bonded propene structures with the lowest ΔG_{Ads} at T4 viewed through the sinusoidal (top) and straight (bottom) channels. $\Delta G_{\text{ads,C3}}$ values are reported at 503 K. $\Delta E_{\text{distort,C3}}$, $\Delta E_{\text{disp,C3}}$, and $\Delta E_{\text{PA+chem,C3}}$ are calculated according to Eqs. 13, 14 and 15, respectively, in the main text.

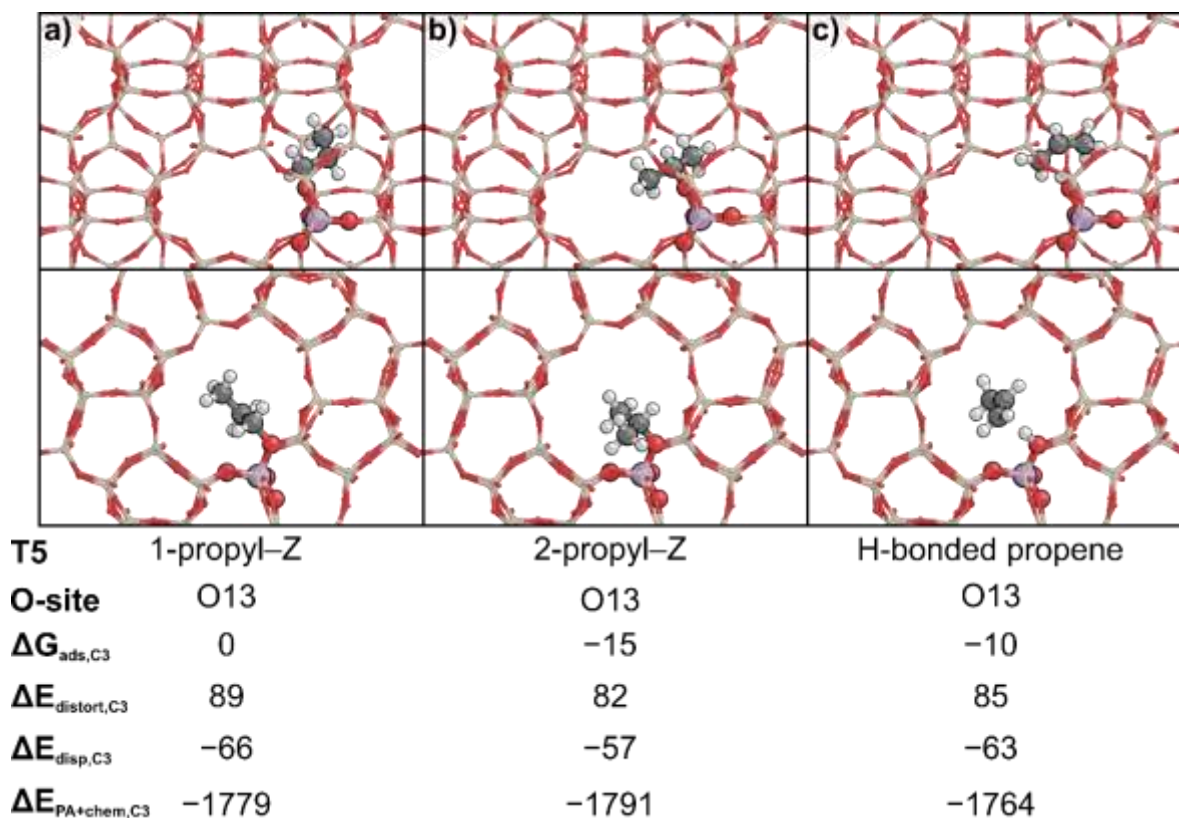


Figure S26. **a)** 1-propyl-Z, **b)** 2-propyl-Z, **c)** and H-bonded propene structures with the lowest ΔG_{Ads} at T5 viewed through the sinusoidal (top) and straight (bottom) channels. $\Delta G_{\text{ads,C3}}$ values are reported at 503 K. $\Delta E_{\text{distort,C3}}$, $\Delta E_{\text{disp,C3}}$, and $\Delta E_{\text{PA+chem,C3}}$ are calculated according to Eqs. 13, 14 and 15, respectively, in the main text.

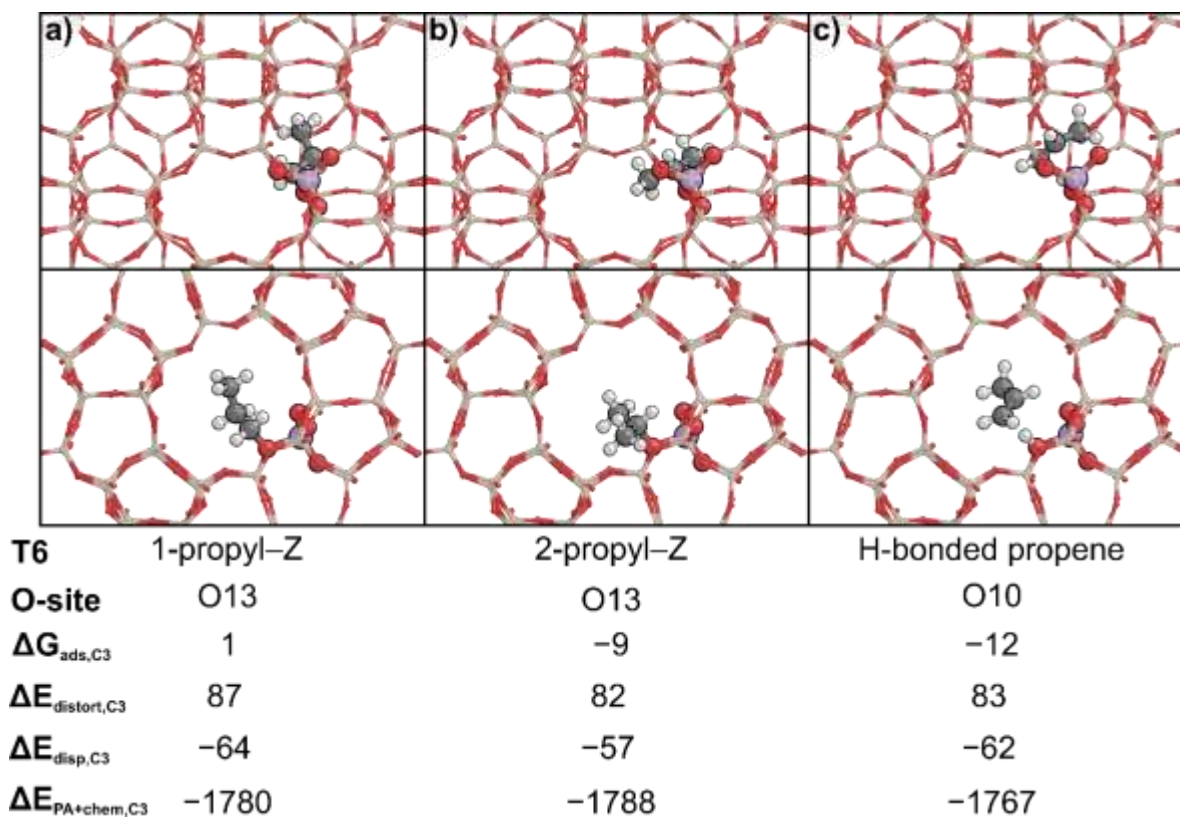


Figure S27. **a)** 1-propyl-Z, **b)** 2-propyl-Z, **c)** and H-bonded propene structures with the lowest ΔG_{Ads} at T6 viewed through the sinusoidal (top) and straight (bottom) channels. $\Delta G_{\text{ads,C3}}$ values are reported at 503 K. $\Delta E_{\text{distort,C3}}$, $\Delta E_{\text{disp,C3}}$, and $\Delta E_{\text{PA+chem,C3}}$ are calculated according to Eqs. 13, 14 and 15, respectively, in the main text.

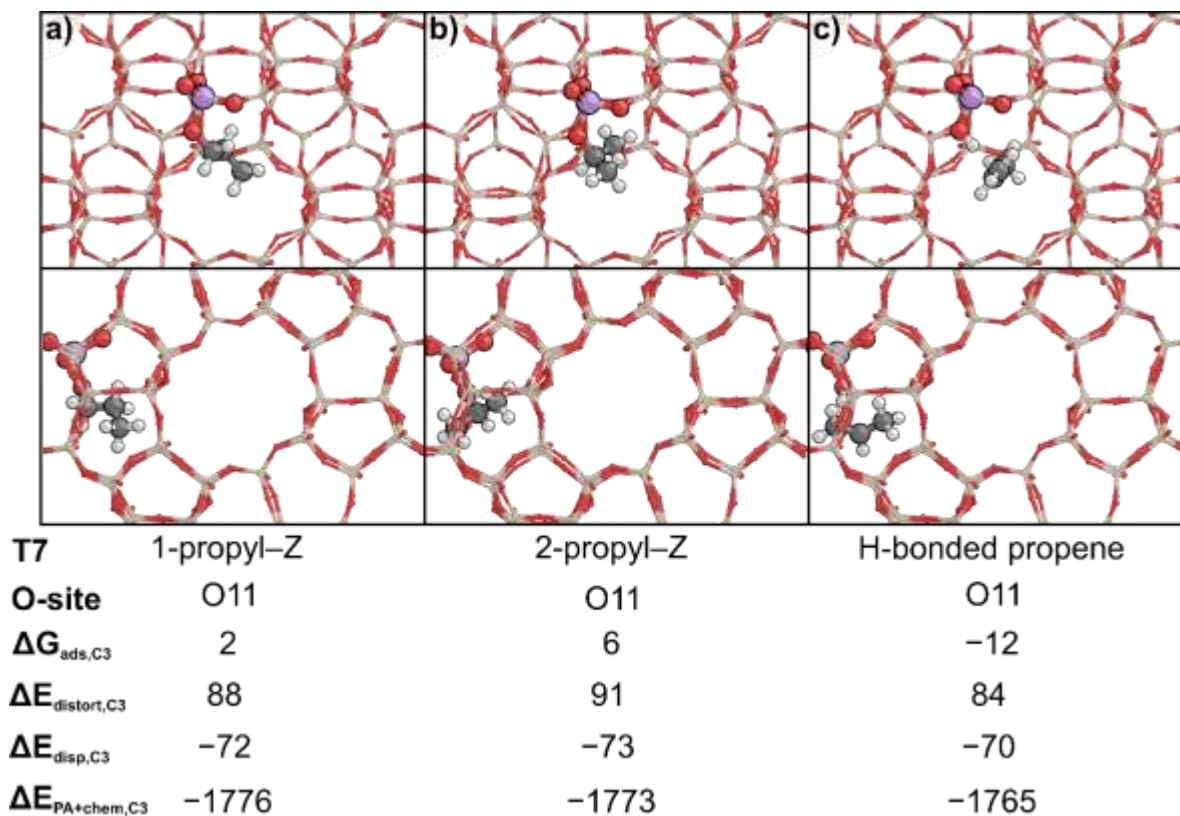


Figure S28. **a)** 1-propyl-Z, **b)** 2-propyl-Z, **c)** and H-bonded propene structures with the lowest ΔG_{Ads} at T7 viewed through the sinusoidal (top) and straight (bottom) channels. $\Delta G_{\text{ads,C3}}$ values are reported at 503 K. $\Delta E_{\text{distort,C3}}$, $\Delta E_{\text{disp,C3}}$, and $\Delta E_{\text{PA+chem,C3}}$ are calculated according to Eqs. 13, 14 and 15, respectively, in the main text.

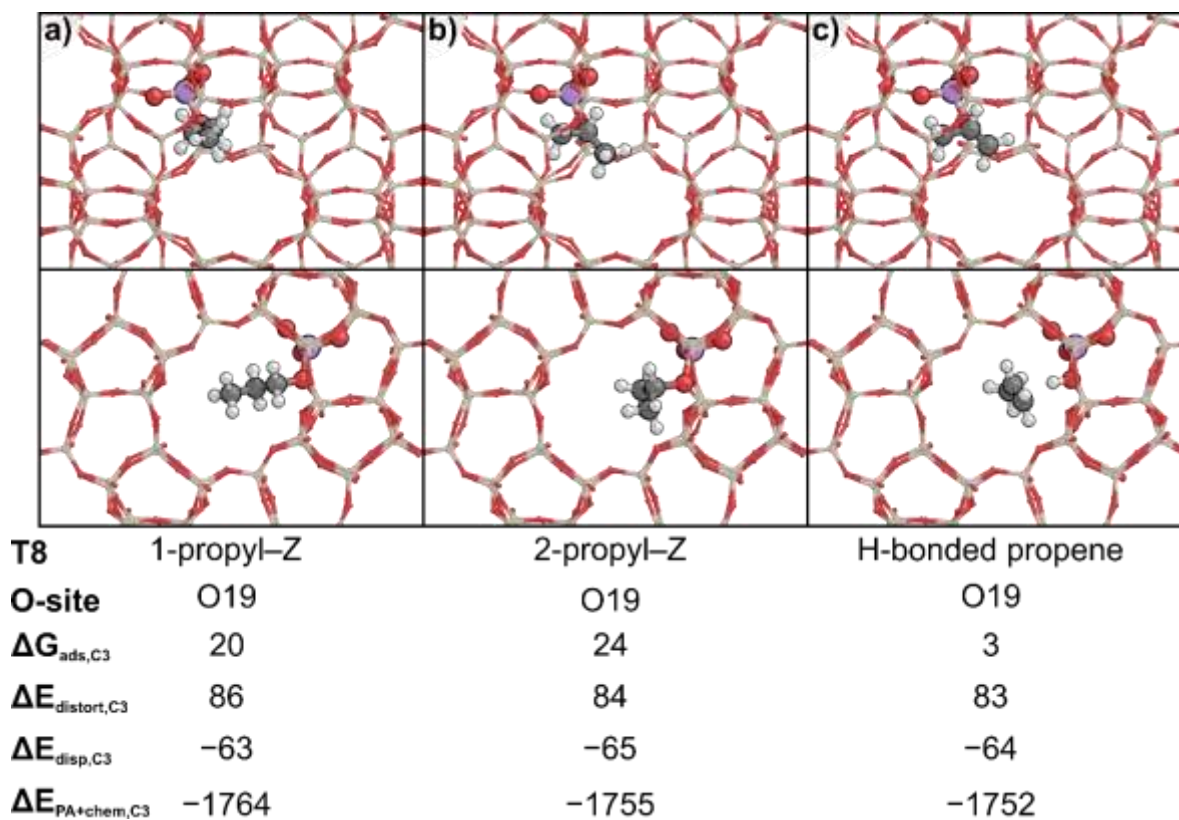


Figure S29. **a)** 1-propyl-Z, **b)** 2-propyl-Z, **c)** and H-bonded propene structures with the lowest ΔG_{Ads} at T8 viewed through the sinusoidal (top) and straight (bottom) channels. $\Delta G_{\text{ads,C3}}$ values are reported at 503 K. $\Delta E_{\text{distort,C3}}$, $\Delta E_{\text{disp,C3}}$, and $\Delta E_{\text{PA+chem,C3}}$ are calculated according to Eqs. 13, 14 and 15, respectively, in the main text.

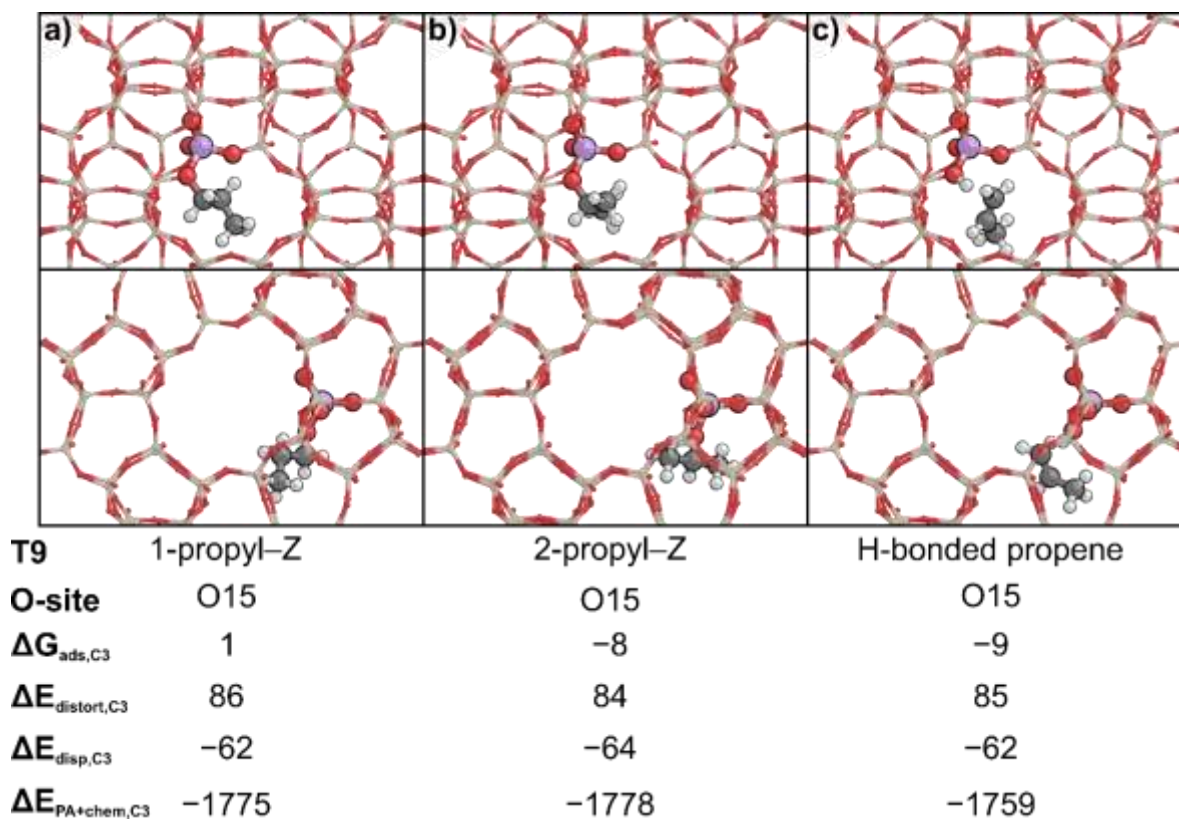


Figure S30. **a)** 1-propyl-Z, **b)** 2-propyl-Z, **c)** and H-bonded propene structures with the lowest ΔG_{Ads} at T9 viewed through the sinusoidal (top) and straight (bottom) channels. $\Delta G_{\text{ads,C3}}$ values are reported at 503 K. $\Delta E_{\text{distort,C3}}$, $\Delta E_{\text{disp,C3}}$, and $\Delta E_{\text{PA+chem,C3}}$ are calculated according to Eqs. 13, 14 and 15, respectively, in the main text.

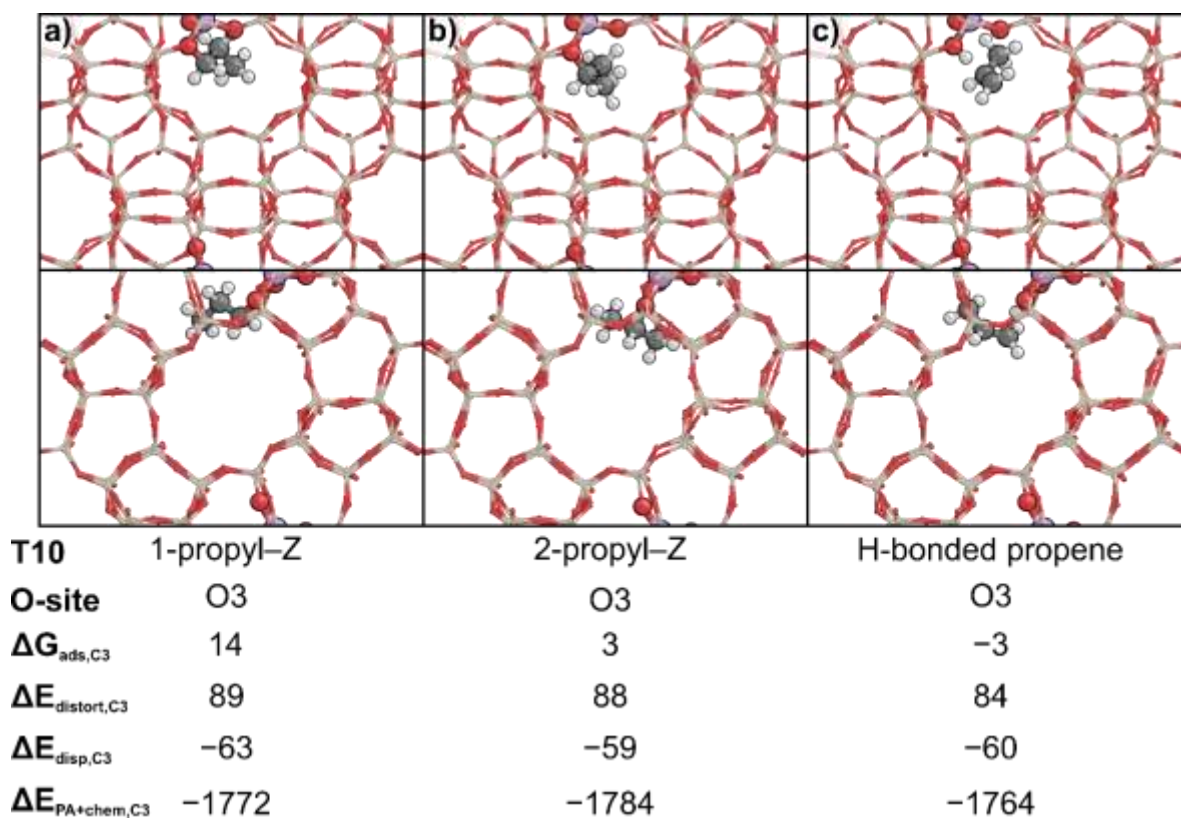


Figure S31. **a)** 1-propyl-Z, **b)** 2-propyl-Z, **c)** and H-bonded propene structures with the lowest ΔG_{Ads} at T10 viewed through the sinusoidal (top) and straight (bottom) channels. $\Delta G_{\text{ads,C3}}$ values are reported at 503 K. $\Delta E_{\text{distort,C3}}$, $\Delta E_{\text{disp,C3}}$, and $\Delta E_{\text{PA+chem,C3}}$ are calculated according to Eqs. 13, 14 and 15, respectively, in the main text.

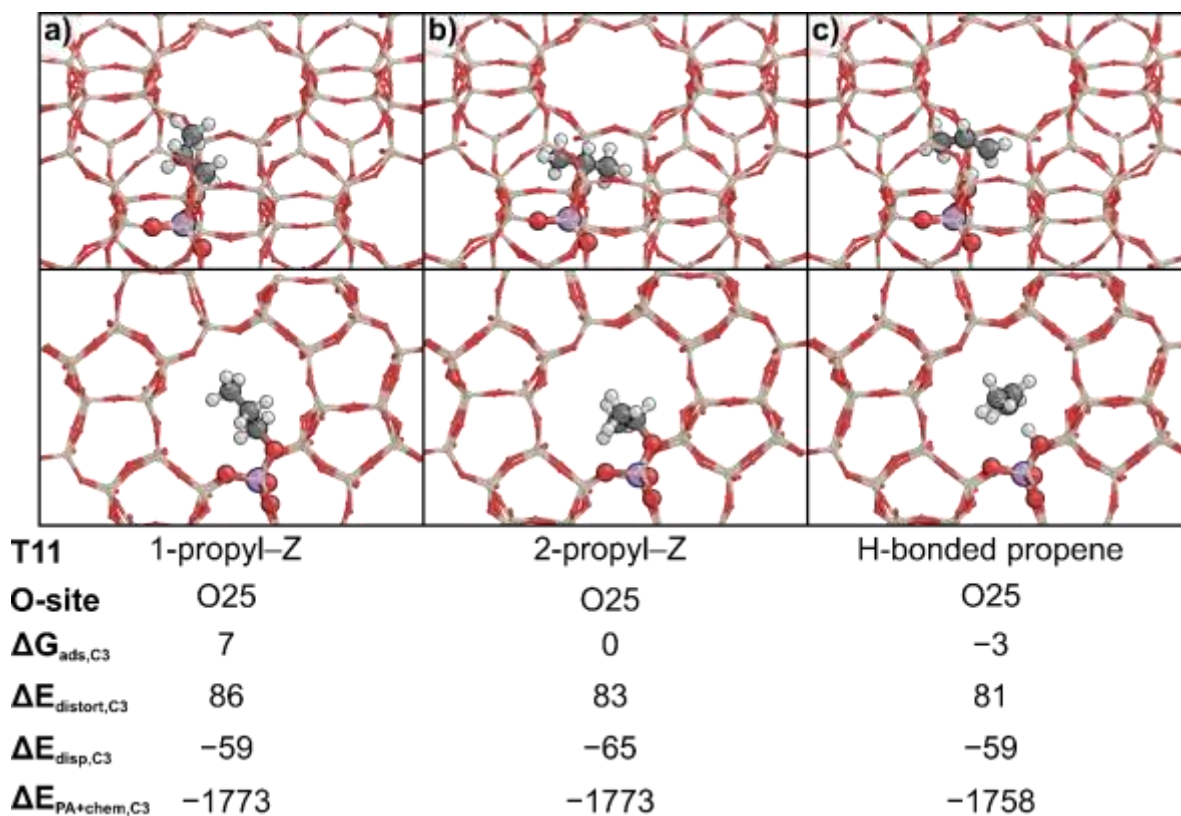


Figure S32. **a)** 1-propyl-Z, **b)** 2-propyl-Z, **c)** and H-bonded propene structures with the lowest ΔG_{Ads} at T11 viewed through the sinusoidal (top) and straight (bottom) channels. $\Delta G_{\text{ads,C3}}$ values are reported at 503 K. $\Delta E_{\text{distort,C3}}$, $\Delta E_{\text{disp,C3}}$, and $\Delta E_{\text{PA+chem,C3}}$ are calculated according to Eqs. 13, 14 and 15, respectively, in the main text.

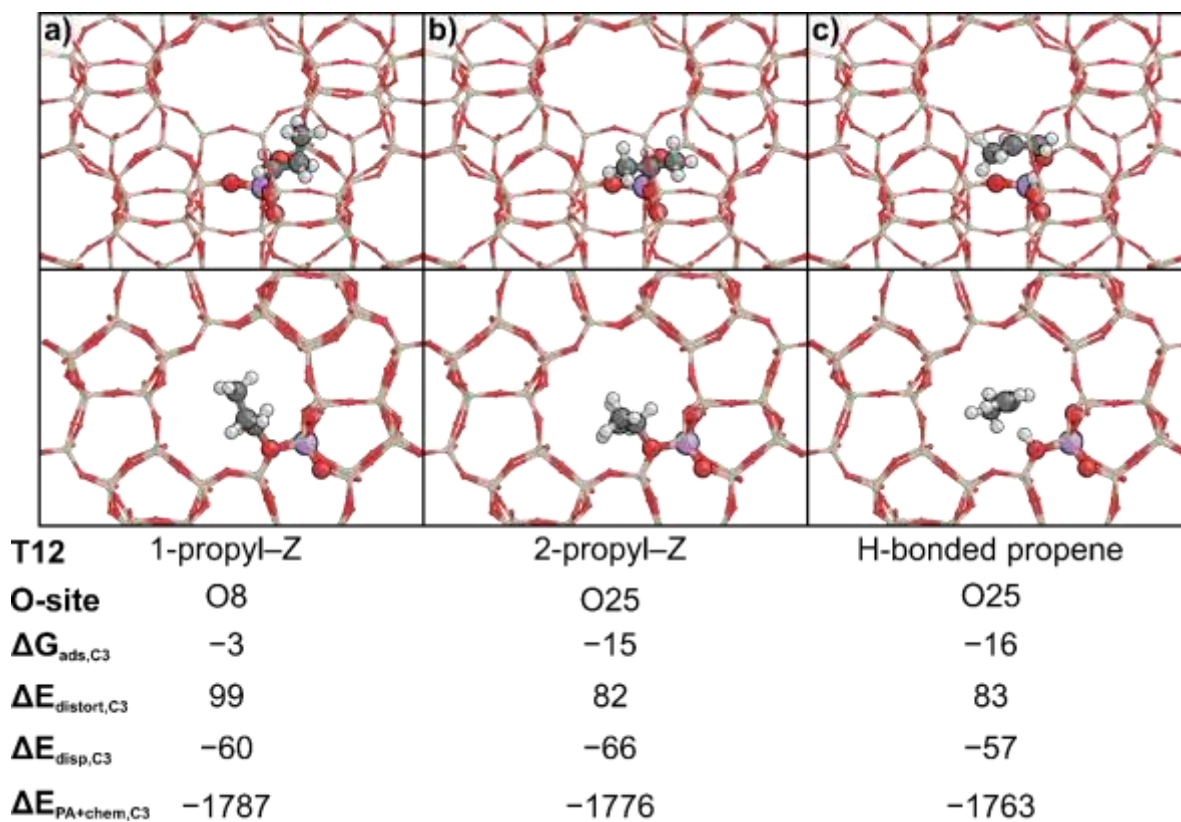


Figure S33. **a)** 1-propyl-Z, **b)** 2-propyl-Z, **c)** and H-bonded propene structures with the lowest ΔG_{Ads} at T12 viewed through the sinusoidal (top) and straight (bottom) channels. $\Delta G_{\text{ads,C3}}$ values are reported at 503 K. $\Delta E_{\text{distort,C3}}$, $\Delta E_{\text{disp,C3}}$, and $\Delta E_{\text{PA+chem,C3}}$ are calculated according to Eqs. 13, 14 and 15, respectively, in the main text.

S12. H-bonded C6 Thermochemical Cycle

The same thermochemical cycle proposed for C₃ adsorption (Scheme 2 in the main text) was applied to C₆ alkene formation (Scheme S1). The corresponding distortion energy, $\Delta E_{\text{distort,C6}}$ (kJ mol⁻¹) was calculated by subtracting the anionic framework energy after removing the C₆ adsorbate relative to the initial anionic framework structure:

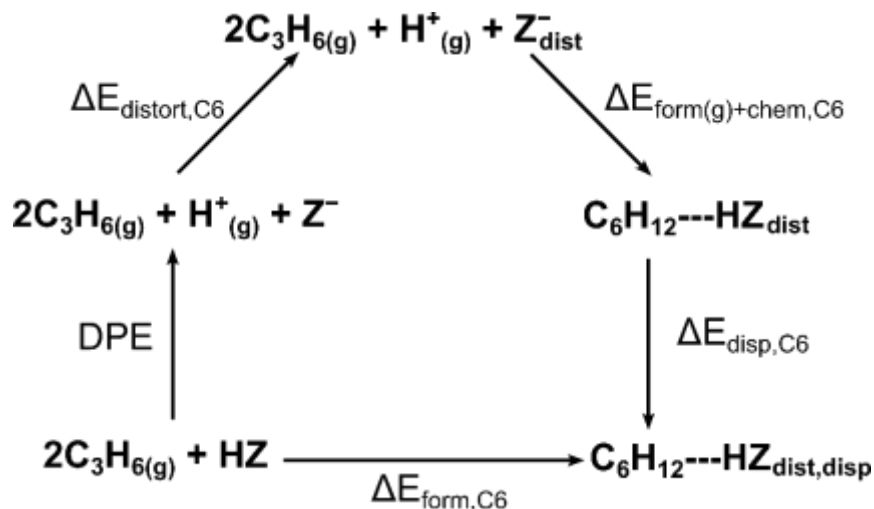
$$\Delta E_{\text{distort,C6}} = E_{\text{C}_6^*,\text{Z}^-} - E_{\text{Z}^-} \quad (\text{S5})$$

and is analogous to $\Delta E_{\text{distort,C3}}$ calculated for C₃ adsorbates (Eqn. 8). The dispersive component of C₆ formation, $\Delta E_{\text{disp,C6}}$ (kJ mol⁻¹), was also calculated:

$$\Delta E_{\text{disp,C6}} = E_{\text{disp,C}_6^*} - (E_{\text{disp,H-Z}} + 2 * E_{\text{disp,C}_3(\text{g})}) \quad (\text{S6})$$

and is similarly comparable to the C₃ analogue, $\Delta E_{\text{disp,C3}}$ (Eqn. 9). Lastly, we subtracted the individual component energies from $\Delta G_{\text{form,C6}}$ to obtain $\Delta E_{\text{PA+chem,C6}}$:

$$\Delta E_{\text{PA+chem,C6}} = \Delta E_{\text{ads,C6}} - \Delta E_{\text{distort,C6}} - \Delta E_{\text{disp,C6}} - \text{DPE} \quad (\text{S7})$$



Scheme S1. Thermochemical cycle for 2 C₃H₆ molecules to adsorb near an acid site as a C₆ H-bonded alkene. DPE is the deprotonation energy of the zeolite framework, $\Delta E_{\text{distort,C6}}$ is the energy to distort the zeolite framework in the presence of the C₆ H-bonded alkene, $\Delta E_{\text{form(g)+chem,C6}}$ is the sum of the energy for 2 C₃H₆ molecules to form C₆H₁₂ in the gas-phase and the chemisorption energy of the alkene, and $\Delta E_{\text{disp,C6}}$ is the dispersive component of the adsorption.

S13. Images of C₆ H-bonded Alkenes at Each T-site

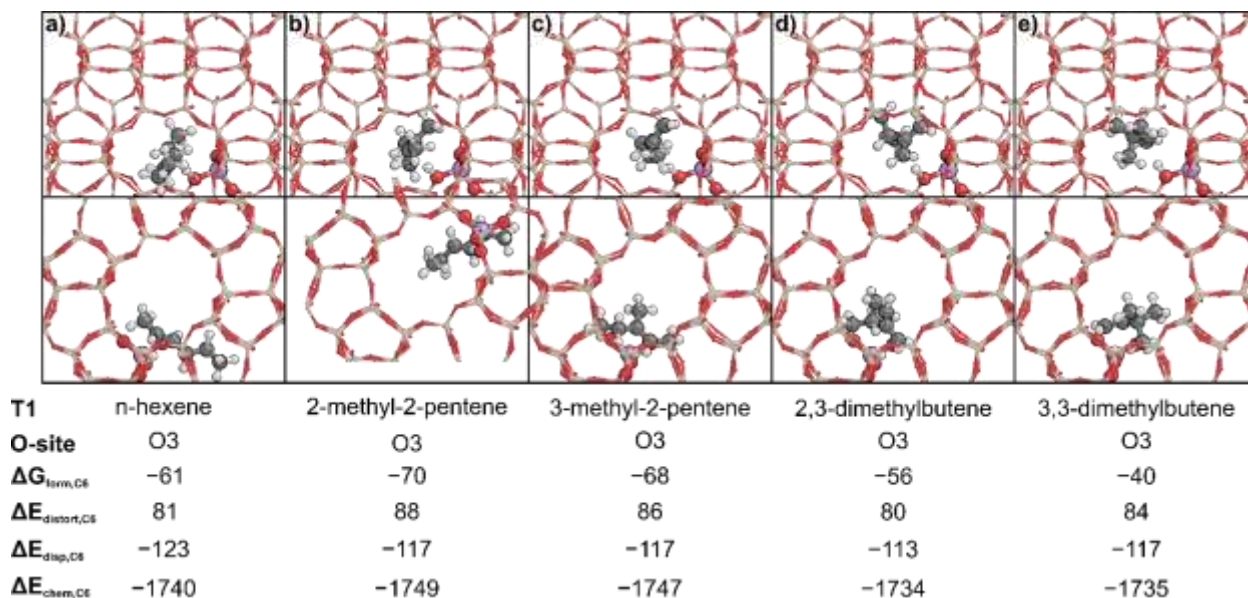


Figure S34. **a)** n-hexene, **b)** 2-methylpentene, **c)** 3-methylpentene, **d)** 2,3-dimethylbutene, and **e)** 3,3-dimethylbutene structures with the lowest $\Delta G_{\text{form,C6}}$ at T1 viewed through the sinusoidal (top) and straight (bottom) channels. $\Delta G_{\text{form,C6}}$ values are reported at 503 K. $\Delta E_{\text{distort,C6}}$, $\Delta E_{\text{disp,C6}}$, and $\Delta E_{\text{chem,C6}}$ are calculated according to Eqns. S5, S6 and S7, respectively, in the main text.

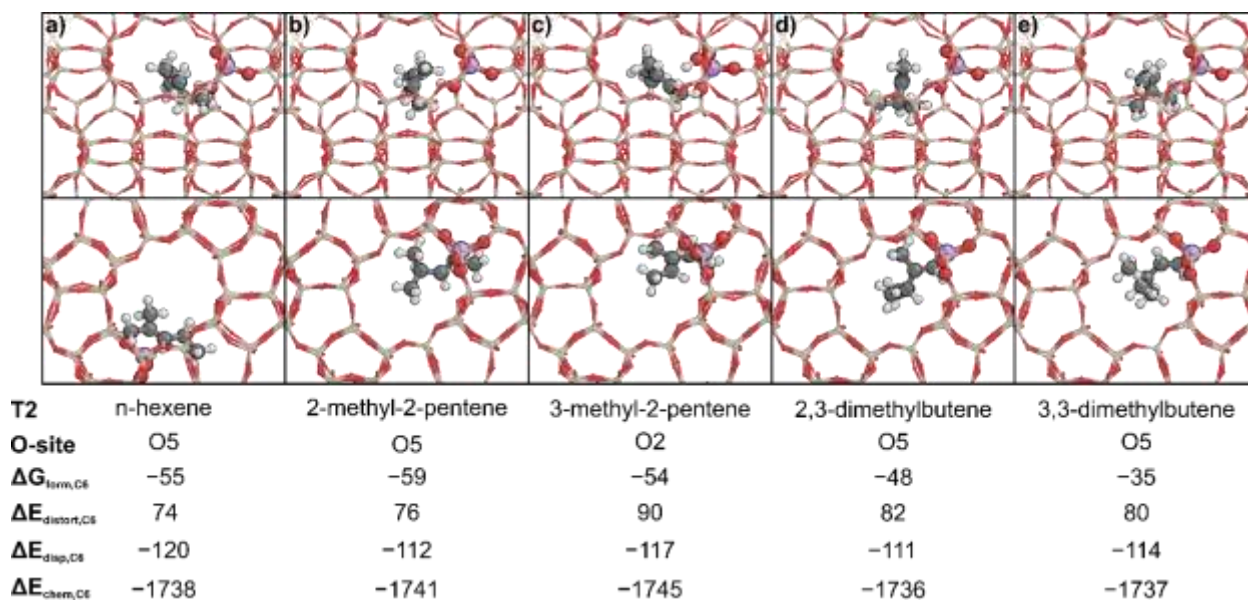


Figure S35. **a)** n-hexene, **b)** 2-methylpentene, **c)** 3-methylpentene, **d)** 2,3-dimethylbutene, and **e)** 3,3-dimethylbutene structures with the lowest $\Delta G_{\text{form,C6}}$ at T2 viewed through the sinusoidal (top) and straight (bottom) channels. $\Delta G_{\text{form,C6}}$ values are reported at 503 K. $\Delta E_{\text{distort,C6}}$, $\Delta E_{\text{disp,C6}}$, and $\Delta E_{\text{chem,C6}}$ are calculated according to Eqns. S5, S6 and S7, respectively, in the main text.

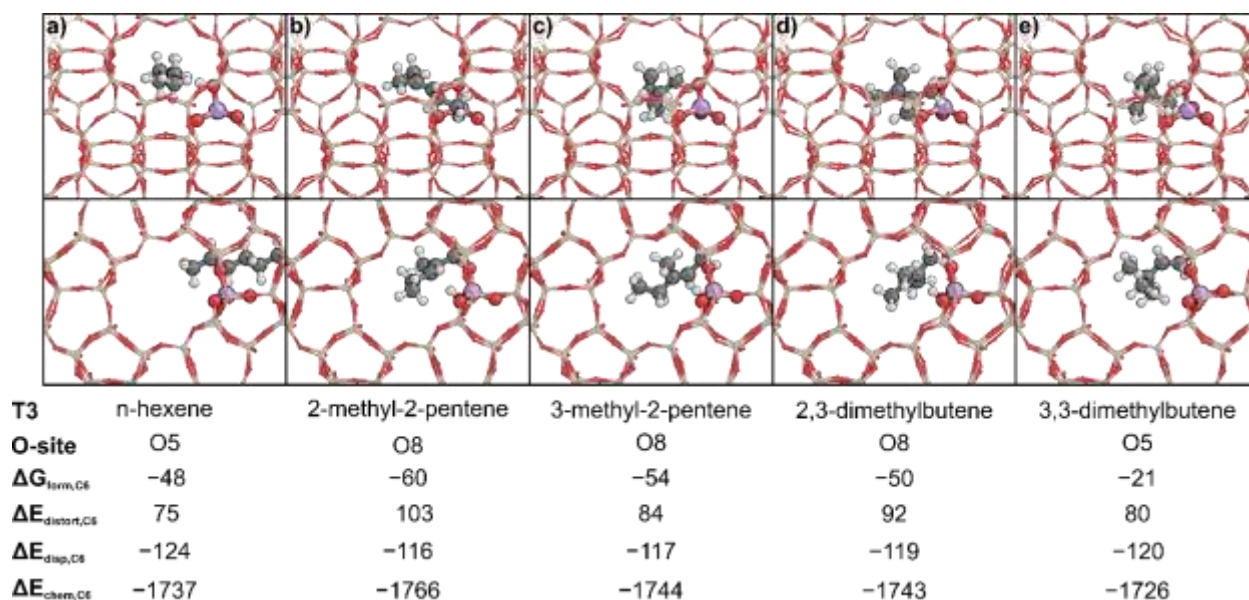


Figure S36. a) n-hexene, b) 2-methylpentene, c) 3-methylpentene, d) 2,3-dimethylbutene, and e) 3,3-dimethylbutene structures with the lowest $\Delta G_{\text{form,C6}}$ at T3 viewed through the sinusoidal (top) and straight (bottom) channels. $\Delta G_{\text{form,C6}}$ values are reported at 503 K. $\Delta E_{\text{distort,C6}}$, $\Delta E_{\text{disp,C6}}$, and $\Delta E_{\text{chem,C6}}$ are calculated according to Eqns. S5, S6 and S7, respectively, in the main text.

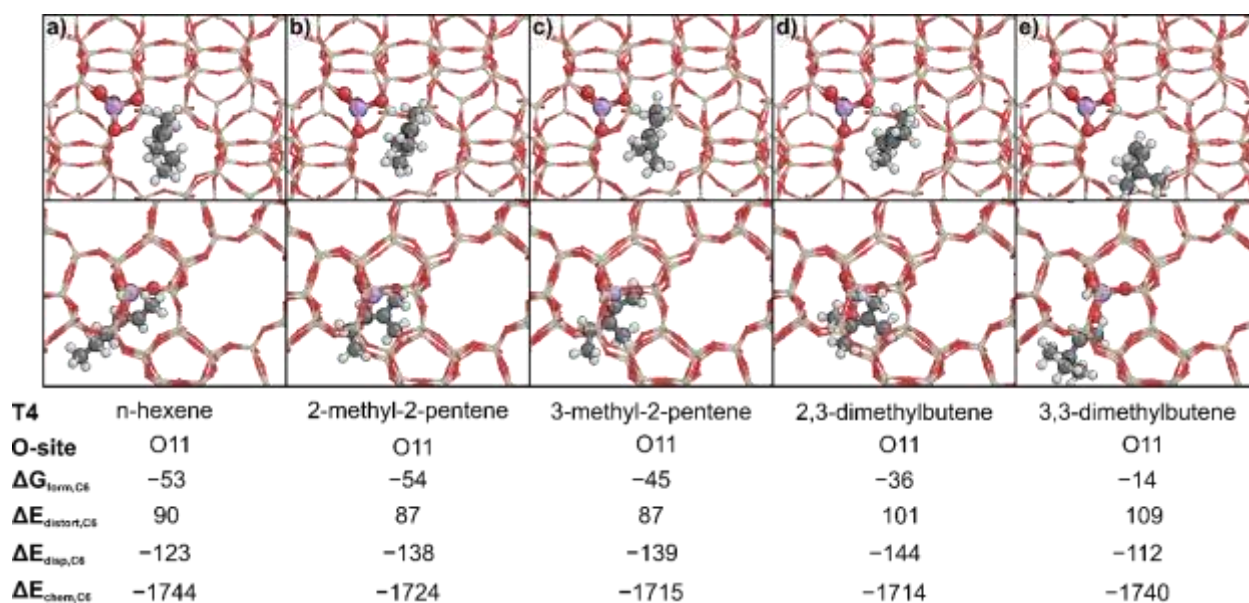
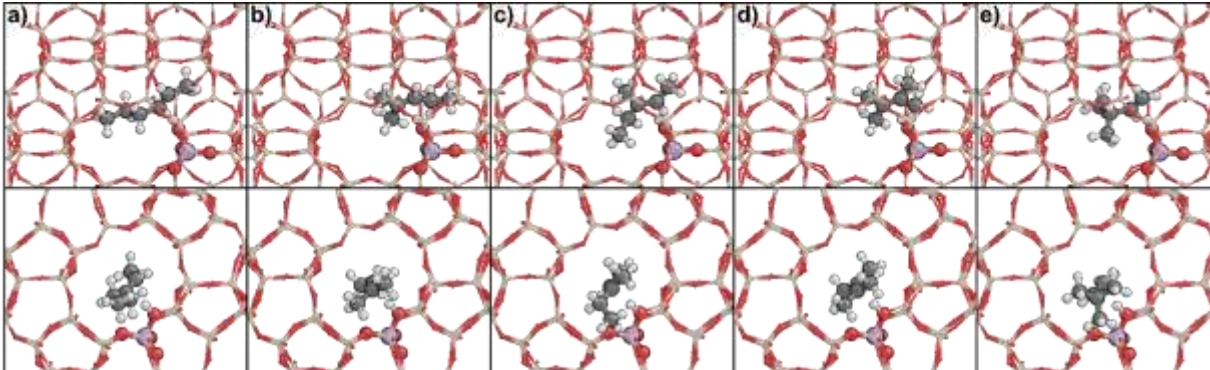
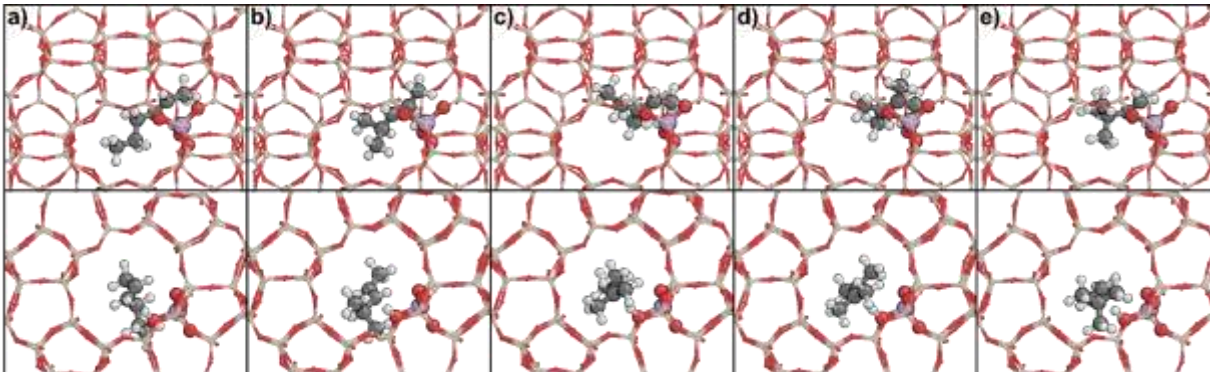


Figure S37. a) n-hexene, b) 2-methylpentene, c) 3-methylpentene, d) 2,3-dimethylbutene, and e) 3,3-dimethylbutene structures with the lowest $\Delta G_{\text{form,C6}}$ at T4 viewed through the sinusoidal (top) and straight (bottom) channels. $\Delta G_{\text{form,C6}}$ values are reported at 503 K. $\Delta E_{\text{distort,C6}}$, $\Delta E_{\text{disp,C6}}$, and $\Delta E_{\text{chem,C6}}$ are calculated according to Eqns. S5, S6 and S7, respectively, in the main text.



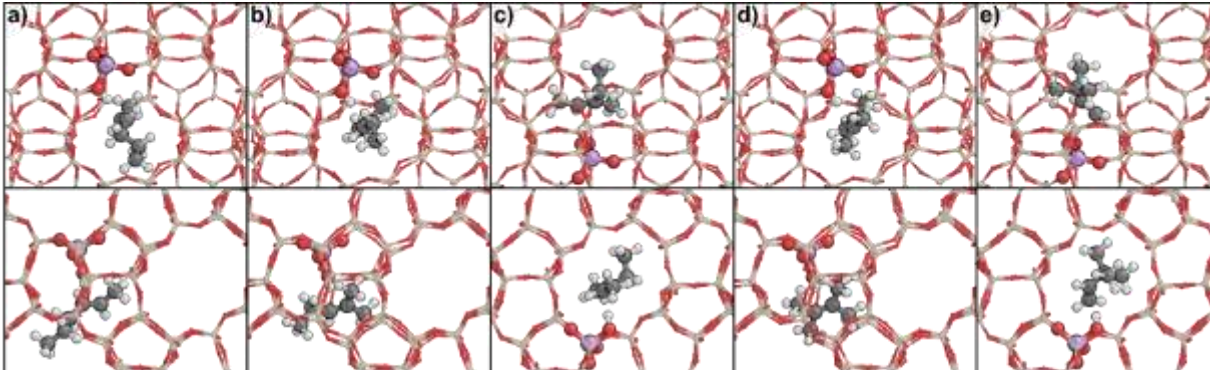
T5	n-hexene	2-methyl-2-pentene	3-methyl-2-pentene	2,3-dimethylbutene	3,3-dimethylbutene
O-site	O13	O13	O13	O13	O13
$\Delta G_{\text{form,C6}}$	-66	-74	-78	-68	-47
$\Delta E_{\text{distort,C6}}$	79	105	82	82	80
$\Delta E_{\text{disp,C6}}$	-112	-123	-119	-130	-124
$\Delta E_{\text{chem,C6}}$	-1755	-1772	-1752	-1731	-1735

Figure S38. **a)** n-hexene, **b)** 2-methylpentene, **c)** 3-methylpentene, **d)** 2,3-dimethylbutene, and **e)** 3,3-dimethylbutene structures with the lowest $\Delta G_{\text{form,C6}}$ at T5 viewed through the sinusoidal (top) and straight (bottom) channels. $\Delta G_{\text{form,C6}}$ values are reported at 503 K. $\Delta E_{\text{distort,C6}}$, $\Delta E_{\text{disp,C6}}$, and $\Delta E_{\text{chem,C6}}$ are calculated according to Eqns. S5, S6 and S7, respectively, in the main text.



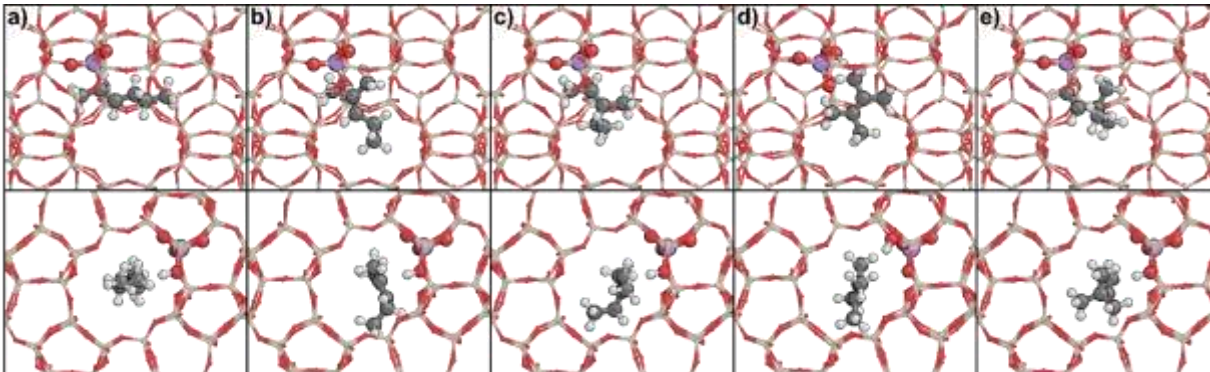
T6	n-hexene	2-methyl-2-pentene	3-methyl-2-pentene	2,3-dimethylbutene	3,3-dimethylbutene
O-site	O13	O13	O13	O13	O13
$\Delta G_{\text{form,C6}}$	-62	-44	-72	-60	-43
$\Delta E_{\text{distort,C6}}$	79	80	78	80	82
$\Delta E_{\text{disp,C6}}$	-117	-113	-119	-128	-113
$\Delta E_{\text{chem,C6}}$	-1750	-1748	-1747	-1733	-1748

Figure S39. **a)** n-hexene, **b)** 2-methylpentene, **c)** 3-methylpentene, **d)** 2,3-dimethylbutene, and **e)** 3,3-dimethylbutene structures with the lowest $\Delta G_{\text{form,C6}}$ at T6 viewed through the sinusoidal (top) and straight (bottom) channels. $\Delta G_{\text{form,C6}}$ values are reported at 503 K. $\Delta E_{\text{distort,C6}}$, $\Delta E_{\text{disp,C6}}$, and $\Delta E_{\text{chem,C6}}$ are calculated according to Eqns. S5, S6 and S7, respectively, in the main text.



T7	n-hexene	2-methyl-2-pentene	3-methyl-2-pentene	2,3-dimethylbutene	3,3-dimethylbutene
O-site	O11	O11	O16	O11	O16
$\Delta G_{\text{form,C6}}$	-53	-46	-57	-43	-5
$\Delta E_{\text{distort,C6}}$	81	108	80	92	93
$\Delta E_{\text{disp,C6}}$	-124	-139	-124	-146	-127
$\Delta E_{\text{chem,C6}}$	-1723	-1739	-1734	-1713	-1718

Figure S40. a) n-hexene, b) 2-methylpentene, c) 3-methylpentene, d) 2,3-dimethylbutene, and e) 3,3-dimethylbutene structures with the lowest $\Delta G_{\text{form,C6}}$ at T7 viewed through the sinusoidal (top) and straight (bottom) channels. $\Delta G_{\text{form,C6}}$ values are reported at 503 K. $\Delta E_{\text{distort,C6}}$, $\Delta E_{\text{disp,C6}}$, and $\Delta E_{\text{chem,C6}}$ are calculated according to Eqns. S5, S6 and S7, respectively, in the main text.



T8	n-hexene	2-methyl-2-pentene	3-methyl-2-pentene	2,3-dimethylbutene	3,3-dimethylbutene
O-site	O19	O19	O19	O17	O19
$\Delta G_{\text{form,C6}}$	-38	-44	-49	-35	-25
$\Delta E_{\text{distort,C6}}$	85	89	82	105	85
$\Delta E_{\text{disp,C6}}$	-122	-123	-117	-116	-117
$\Delta E_{\text{chem,C6}}$	-1730	-1724	-1734	-1732	-1730

Figure S41. a) n-hexene, b) 2-methylpentene, c) 3-methylpentene, d) 2,3-dimethylbutene, and e) 3,3-dimethylbutene structures with the lowest $\Delta G_{\text{form,C6}}$ at T8 viewed through the sinusoidal (top) and straight (bottom) channels. $\Delta G_{\text{form,C6}}$ values are reported at 503 K. $\Delta E_{\text{distort,C6}}$, $\Delta E_{\text{disp,C6}}$, and $\Delta E_{\text{chem,C6}}$ are calculated according to Eqns. S5, S6 and S7, respectively, in the main text.

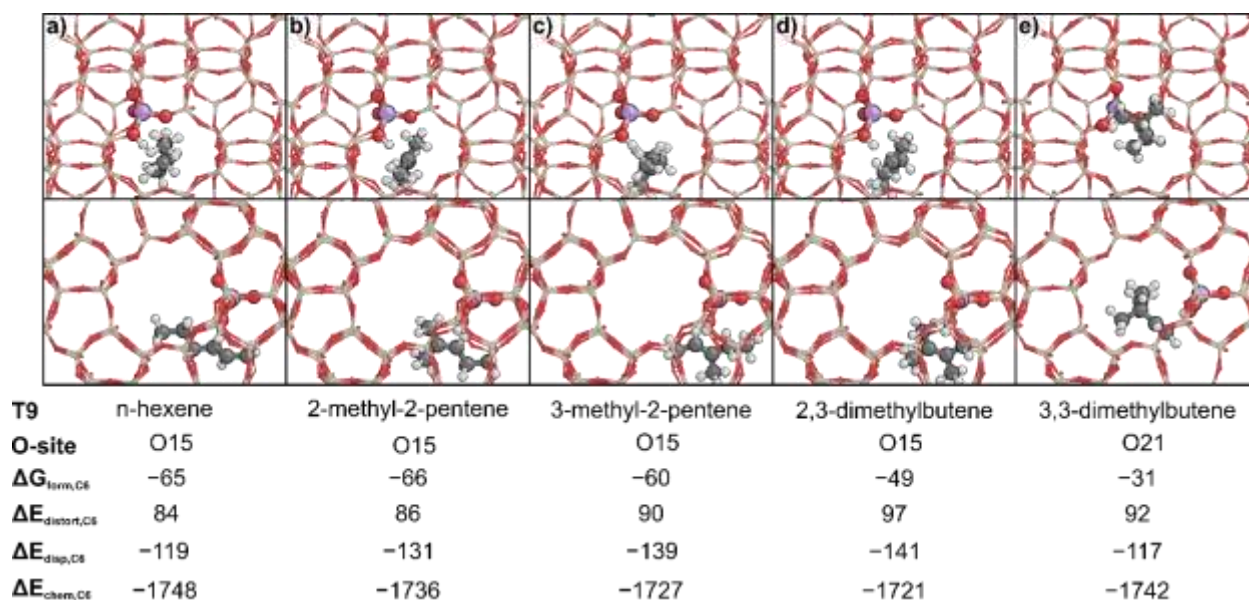


Figure S42. a) n-hexene, b) 2-methylpentene, c) 3-methylpentene, d) 2,3-dimethylbutene, and e) 3,3-dimethylbutene structures with the lowest $\Delta G_{\text{form,C6}}$ at T9 viewed through the sinusoidal (top) and straight (bottom) channels. $\Delta G_{\text{form,C6}}$ values are reported at 503 K. $\Delta E_{\text{distort,C6}}$, $\Delta E_{\text{disp,C6}}$, and $\Delta E_{\text{chem,C6}}$ are calculated according to Eqns. S5, S6 and S7, respectively, in the main text.

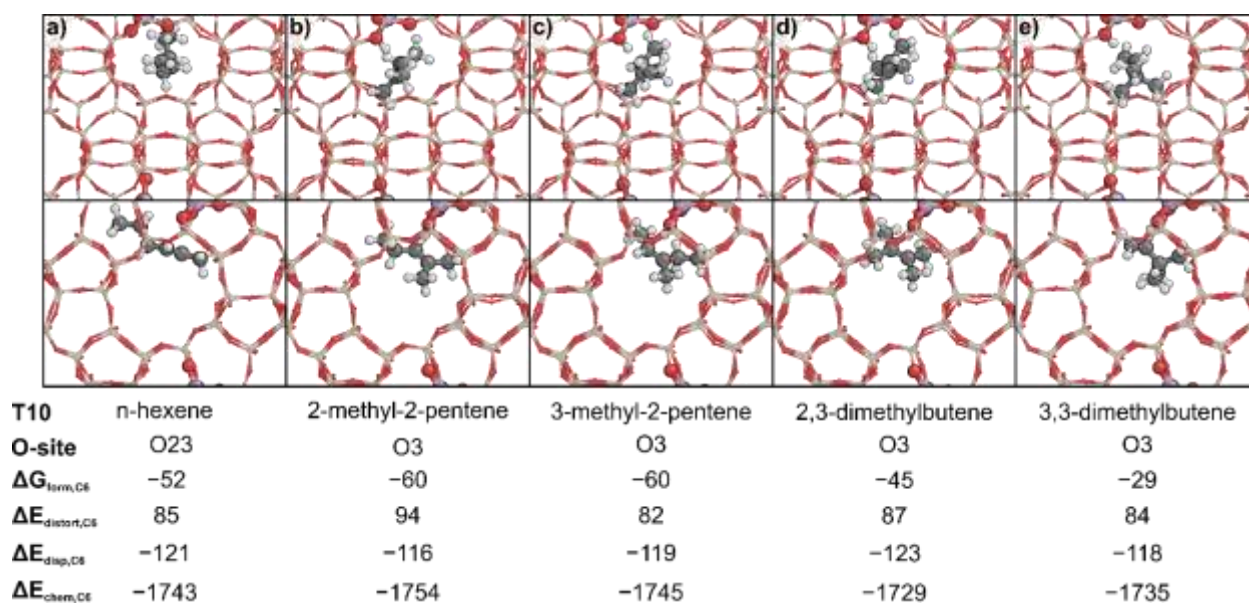


Figure S43. a) n-hexene, b) 2-methylpentene, c) 3-methylpentene, d) 2,3-dimethylbutene, and e) 3,3-dimethylbutene structures with the lowest $\Delta G_{\text{form,C6}}$ at T10 viewed through the sinusoidal (top) and straight (bottom) channels. $\Delta G_{\text{form,C6}}$ values are reported at 503 K. $\Delta E_{\text{distort,C6}}$, $\Delta E_{\text{disp,C6}}$, and $\Delta E_{\text{chem,C6}}$ are calculated according to Eqns. S5, S6 and S7, respectively, in the main text.

	a)	b)	c)	d)	e)
T11	n-hexene	2-methyl-2-pentene	3-methyl-2-pentene	2,3-dimethylbutene	3,3-dimethylbutene
O-site	O25	O25	O25	O25	O25
$\Delta G_{\text{form,C6}}$	-50	-65	-68	-58	-32
$\Delta E_{\text{distort,C6}}$	78	80	77	79	82
$\Delta E_{\text{disp,C6}}$	-116	-123	-119	-128	-113
$\Delta E_{\text{chem,C6}}$	-1738	-1735	-1740	-1723	-1734

Figure S44. **a)** n-hexene, **b)** 2-methylpentene, **c)** 3-methylpentene, **d)** 2,3-dimethylbutene, and **e)** 3,3-dimethylbutene structures with the lowest $\Delta G_{\text{form,C6}}$ at T11 viewed through the sinusoidal (top) and straight (bottom) channels. $\Delta G_{\text{form,C6}}$ values are reported at 503 K. $\Delta E_{\text{distort,C6}}$, $\Delta E_{\text{disp,C6}}$, and $\Delta E_{\text{chem,C6}}$ are calculated according to Eqns. S5, S6 and S7, respectively, in the main text.

	a)	b)	c)	d)	e)
T12	n-hexene	2-methyl-2-pentene	3-methyl-2-pentene	2,3-dimethylbutene	3,3-dimethylbutene
O-site	O25	O25	O25	O25	O25
$\Delta G_{\text{form,C6}}$	-62	-73	-78	-66	-38
$\Delta E_{\text{distort,C6}}$	80	78	75	78	83
$\Delta E_{\text{disp,C6}}$	-120	-123	-120	-131	-117
$\Delta E_{\text{chem,C6}}$	-1739	-1733	-1739	-1722	-1729

Figure S45. **a)** n-hexene, **b)** 2-methylpentene, **c)** 3-methylpentene, **d)** 2,3-dimethylbutene, and **e)** 3,3-dimethylbutene structures with the lowest $\Delta G_{\text{form,C6}}$ at T12 viewed through the sinusoidal (top) and straight (bottom) channels. $\Delta G_{\text{form,C6}}$ values are reported at 503 K. $\Delta E_{\text{distort,C6}}$, $\Delta E_{\text{disp,C6}}$, and $\Delta E_{\text{chem,C6}}$ are calculated according to Eqns. S5, S6 and S7, respectively, in the main text.

S14. Propene Dimerization Transition State Structure

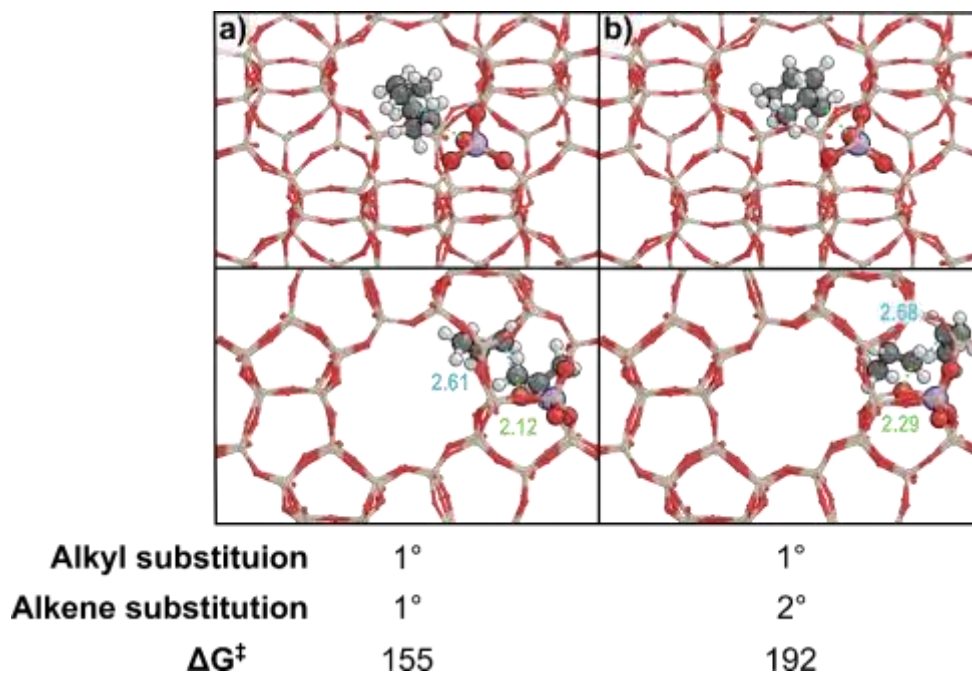


Figure S46. Propene dimerization transition state between a primary (1°) alkyl (1-propyl-Z) and the **a)** primary (1°) and **b)** secondary (2°) carbon of propene. Reported ΔG^\ddagger values are at 503 K. The transition states are located at O9/T4. The distance between the alkyl carbocation C and the alkene C (C-C distance, Å) is indicated in light blue and the distance between the alkyl carbocation and the O-site (C-O distance, Å) is indicated in light green.

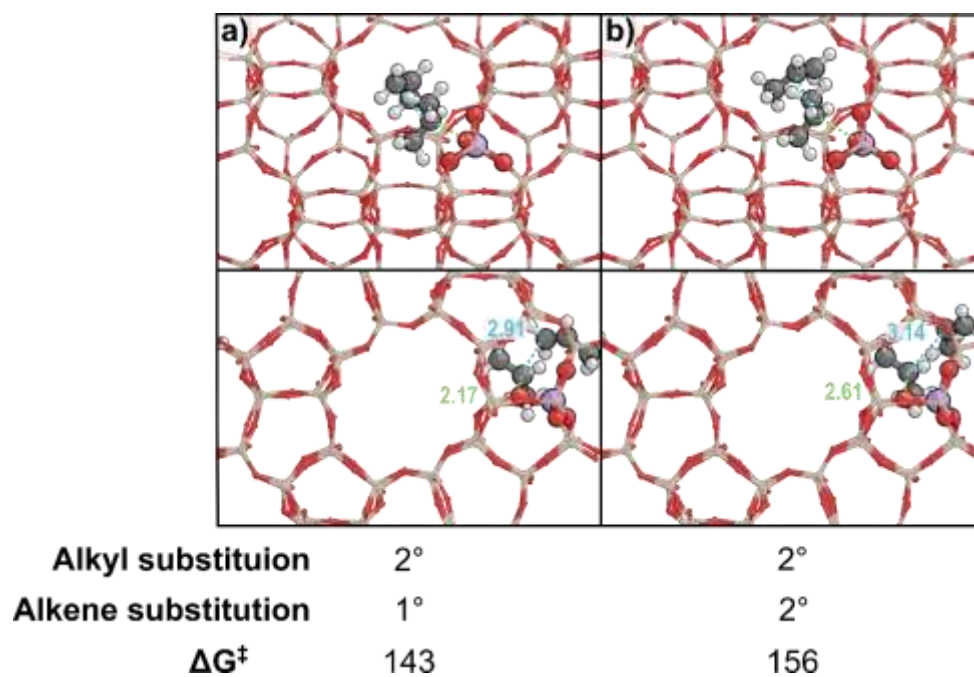


Figure S47. Propene dimerization transition state between a secondary (2°) alkyl (2-propyl-Z) and the **a)** primary (1°) and **b)** secondary (2°) carbon of propene. Reported ΔG^\ddagger values are at 503 K. The transition states are located at O9/T4. The distance between the alkyl carbocation C and the alkene C (C-C distance, Å) is indicated in light blue and the distance between the alkyl carbocation and the O-site (C-O distance, Å) is indicated in light green.

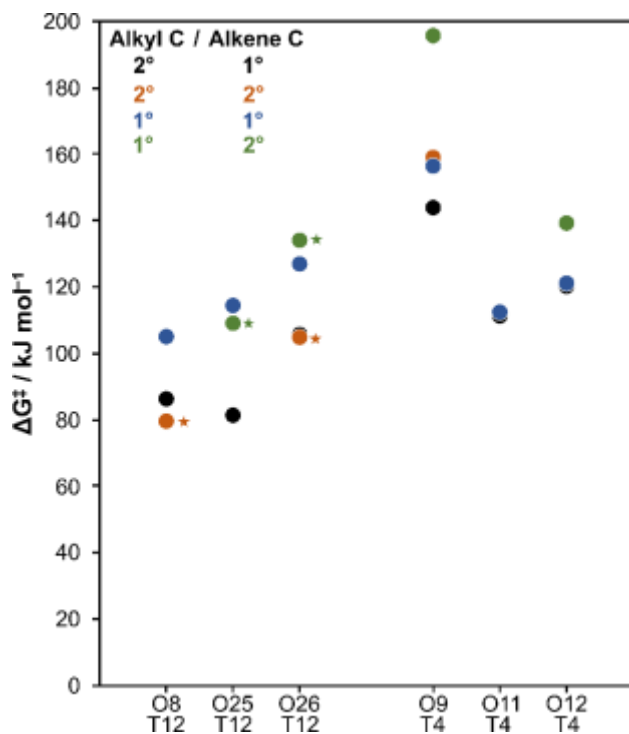


Figure S48. ΔG^\ddagger for the dimerization transition state with **a)** a 2° alkyl C/1° alkene C (black), **b)** a 2° alkyl C/2° alkene C (orange), **c)** a 1° alkyl C/1° alkene C (blue), and **d)** a 1° alkyl C/2° alkene C (green) at the accessible O-sites at T12 and T4. Stars indicate transition state structures where the distance between the carbocation C and the 1° and 2° alkene C are the same.

S15. Images of Transition State at Each T-site

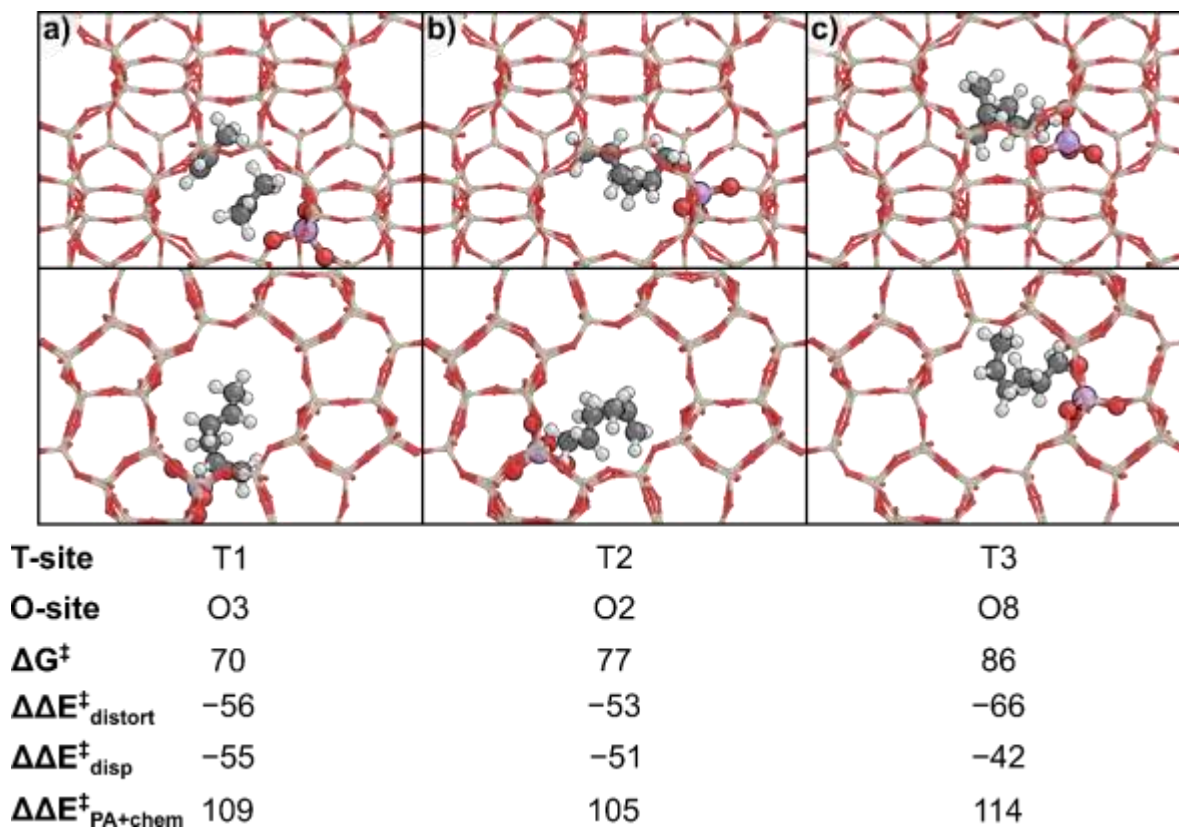


Figure S49. Propene dimerization transition state structure with the lowest ΔG^\ddagger at **a)** T1, **b)** T2, and **c)** T3. ΔG^\ddagger values (Eq. 9 in the main text) are reported at 503 K. $\Delta\Delta E^\ddagger_{\text{distort}}$, $\Delta\Delta E^\ddagger_{\text{disp}}$, and $\Delta\Delta E^\ddagger_{\text{PA+chem}}$ are calculated according to Eqs. 16, 17, and 18 respectively, in Section 3.4 of the main text.

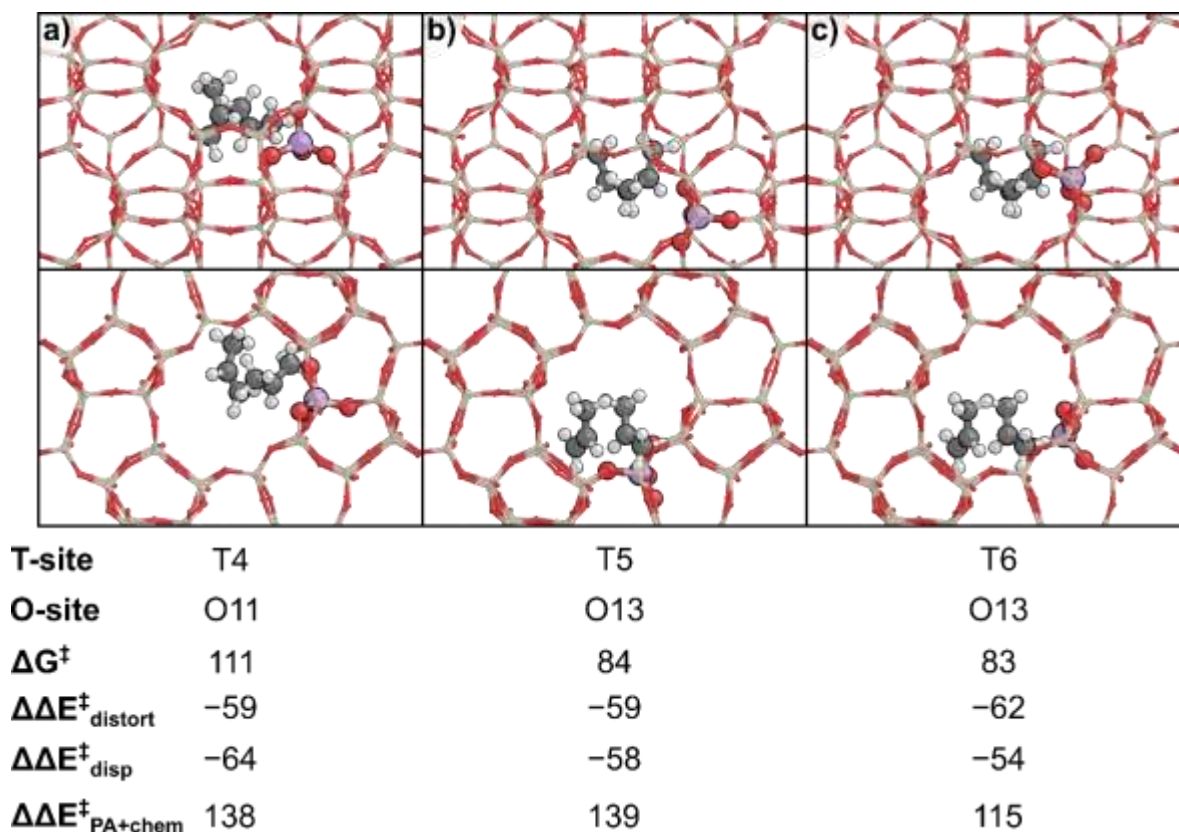


Figure S50. Propene dimerization transition state structure with the lowest ΔG^\ddagger at **a)** T4, **b)** T5, and **c)** T6. ΔG^\ddagger values (Eq. 9 in the main text) are reported at 503 K. $\Delta\Delta E^\ddagger_{\text{distort}}$, $\Delta\Delta E^\ddagger_{\text{disp}}$, and $\Delta\Delta E^\ddagger_{\text{PA+chem}}$ are calculated according to Eqs. 16, 17, and 18 respectively, in Section 3.4 of the main text.

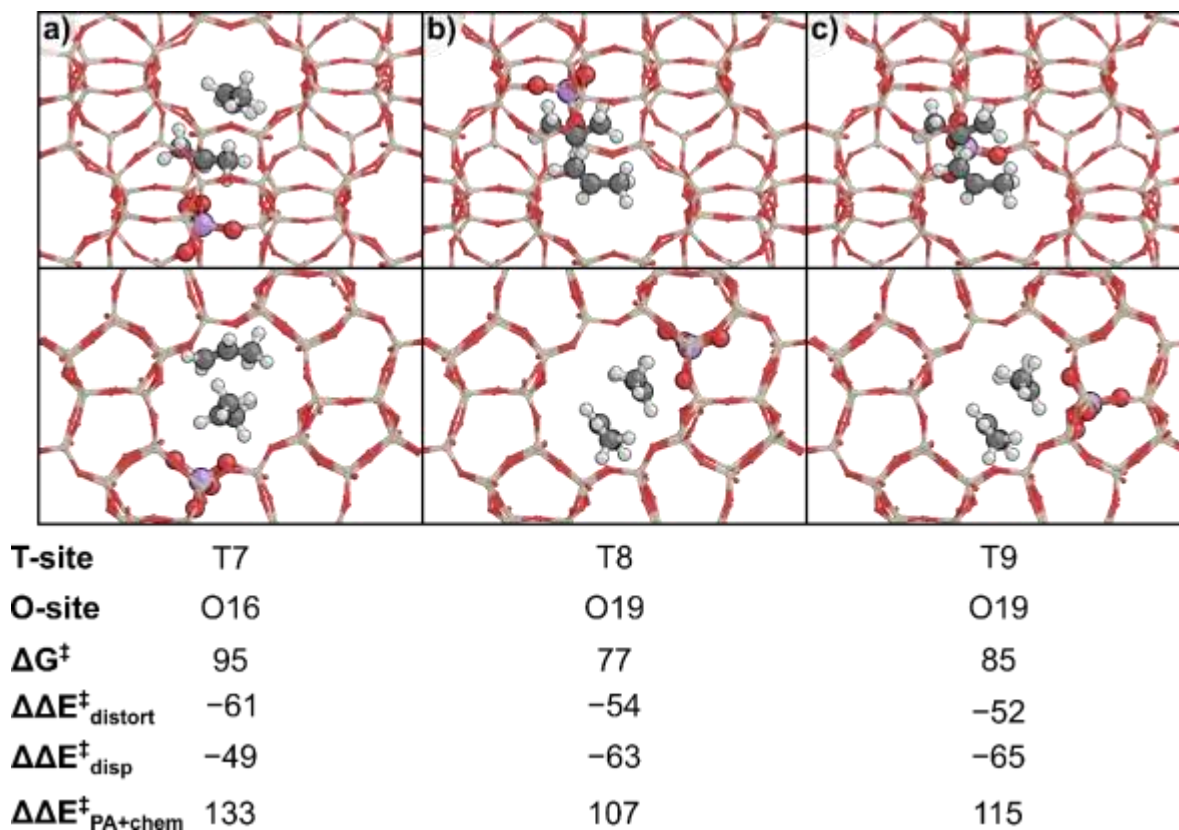


Figure S51. Propene dimerization transition state structure with the lowest ΔG^\ddagger at **a)** T1, **b)** T2, and **c)** T3. ΔG^\ddagger values (Eq. 9 in the main text) are reported at 503 K. $\Delta\Delta E^\ddagger_{\text{distort}}$, $\Delta\Delta E^\ddagger_{\text{disp}}$, and $\Delta\Delta E^\ddagger_{\text{PA+chem}}$ are calculated according to Eqs. 16, 17, and 18 respectively, in Section 3.4 of the main text.

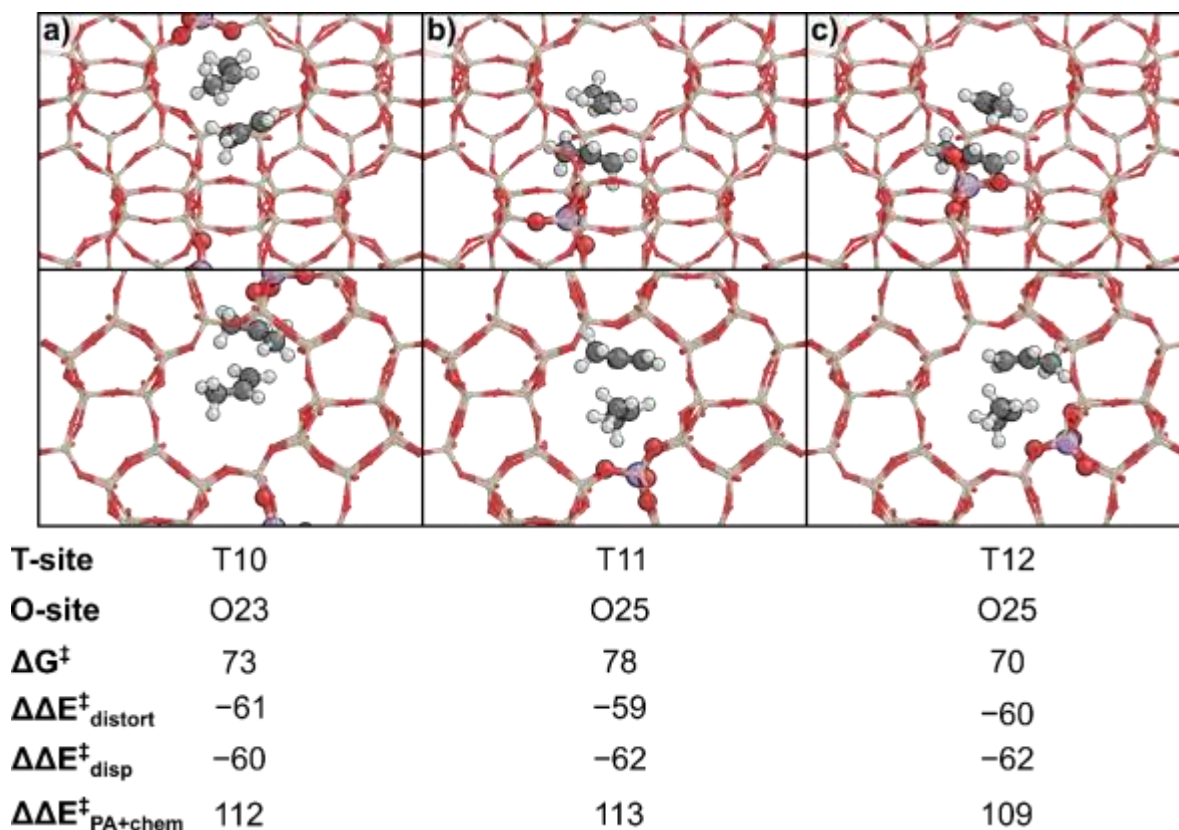


Figure S52. Propene dimerization transition state structure with the lowest ΔG^\ddagger at **a)** T1, **b)** T2, and **c)** T3. ΔG^\ddagger values (Eq. 9 in the main text) are reported at 503 K. $\Delta\Delta E^\ddagger_{\text{distort}}$, $\Delta\Delta E^\ddagger_{\text{disp}}$, and $\Delta\Delta E^\ddagger_{\text{PA+chem}}$ are calculated according to Eqs. 16, 17, and 18 respectively, in Section 3.4 of the main text.

S16. Second Order Effective Free Energy Barriers

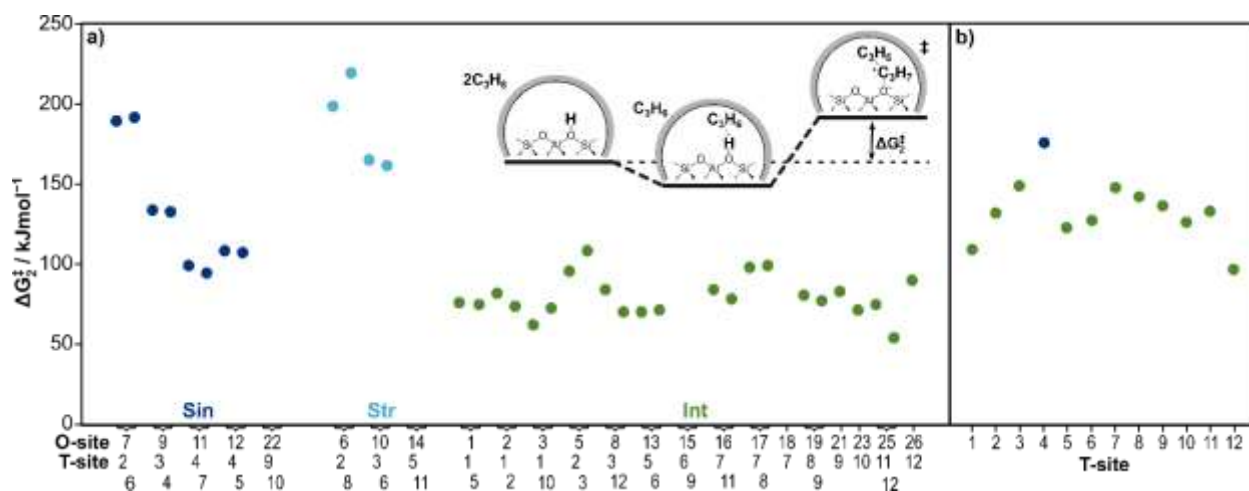
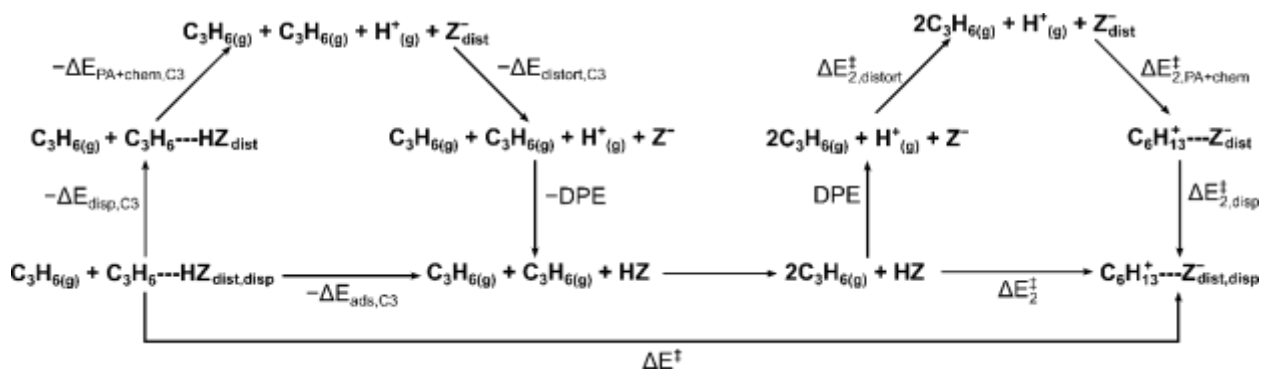


Figure S53. a) Effective second order free energy barriers ($\Delta G_{2^\ddagger}^\ddagger$, kJ mol^{-1} , Eqn. 15) relative to the protonated acid site and gas phase propene in the sinusoidal channel (dark blue), straight channel (light blue), and intersection (green) at 503 K. Average $\Delta G_{2^\ddagger}^\ddagger$ in each environment is denoted with dashed lines. **b)** The lowest $\Delta G_{2^\ddagger}^\ddagger$ per T-site.

S17. Propene Dimerization Transition State Thermochemical Cycle



Scheme S2. The thermochemical cycle for the transition state effective barrier (ΔE^\ddagger) relative to H-bonded propene. The first half of the cycle is the reverse of the thermochemical cycle for the adsorption of C_3 (Scheme 1) with a gas-phase propene. The second cycle is the thermochemical cycle for the transition state formation relative to a protonated surface, which corresponds to the second order effective barrier (ΔE_{2^\ddagger}). The individual components of the effective barrier relative to C_3 are equal to the sum of the component in the reverse C_3 cycle and the component in the second order transition state cycle.

S18. Acid Site Distortion and Adsorbate-Acid Site Interaction Distance

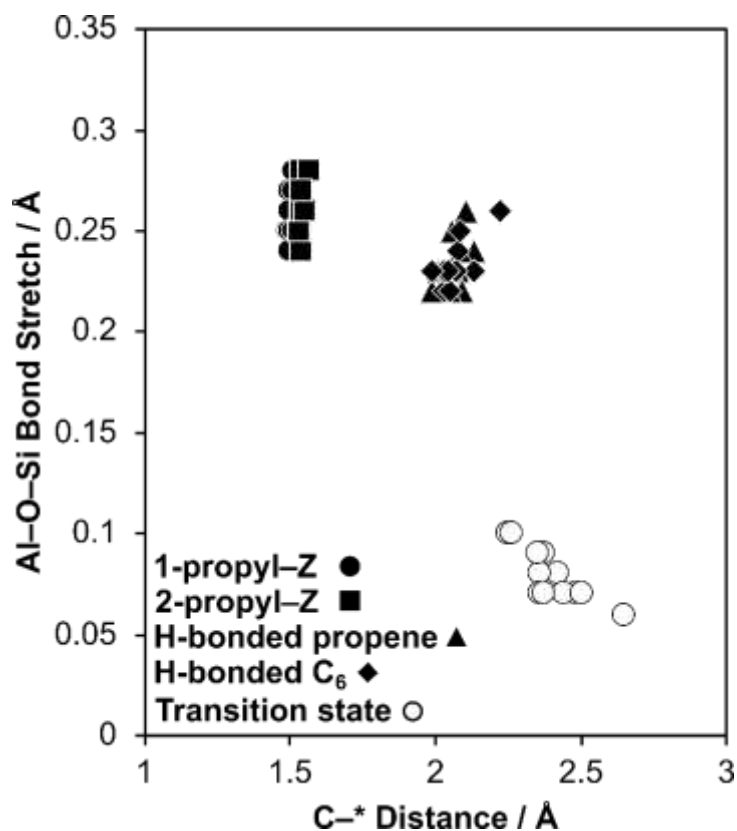


Figure S54. Al–O–Si bond stretch (Å), calculated as the sum of the Al–O and O–Si bonds of the adsorbate referenced to the sum of the bond distances in the empty framework at the corresponding O-site, versus C–* distance (Å). For surface bound alkyls, C–* is the length of the covalent bond between the bound C atom and the O-site. For H-bonded alkenes, C–* is the average distance between the two C atoms of the pi bond and the proton bound to the O-site. For the transition state, C–* is the distance between the carbenium C atom and the O-site.

S19. Propene Dimerization Step Pressure and Step Temperature Experiments

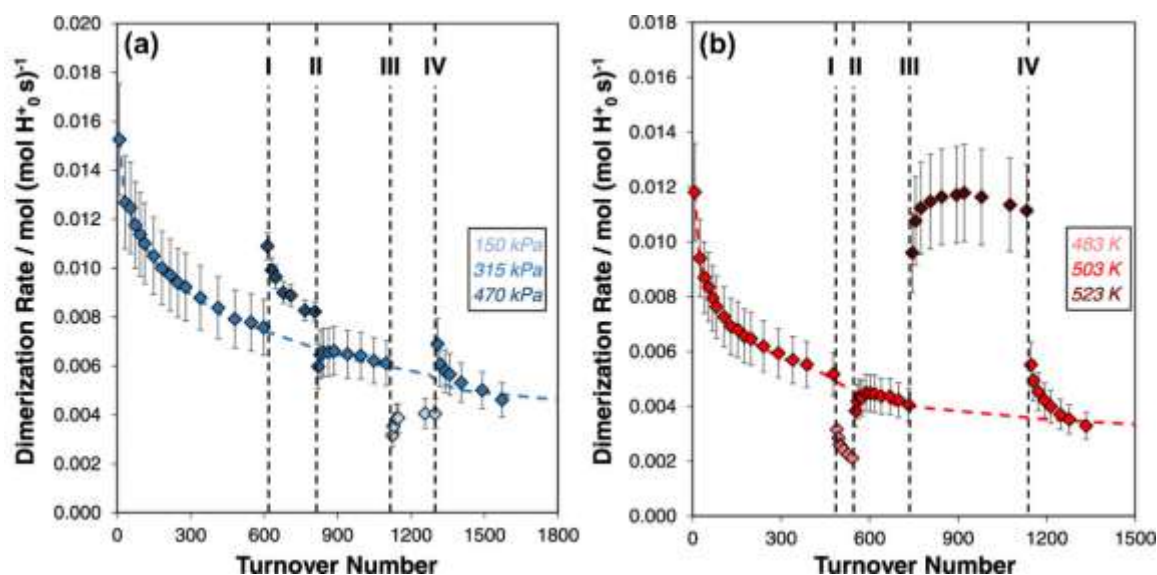


Figure S55. a) Propene dimerization rates measured on MFI-TPA-0.33 at 503 K. Blue dashed lines are interpolated rates at 315 kPa C₃H₆. Black dashed lines signify step-chnges in pressure: (I) 315 → 470 kPa, (II) 470 → 315 kPa, (III) 315 → 150 kPa, (IV) 150 → 315 kPa. b) Propene dimerization rates measured on MFI-TPA-0.33 at 315 kPa C₃H₆. Red dashed lines are interpolated rates at 503 K. Black dashed lines signify step-changes in temperature. (I) 503 → 483 K, (II) 483 → 503 K, (III) 503 → 523 K, (IV) 523 → 503 K. Error bars reflect absolute error. Reproduced from Bickel et al.¹ Copyright 2023 American Chemical Society.

S20. Analysis of Product Selectivity Between MFI Samples of Different H⁺-site Location

MFI-DABCO samples showed higher $(k_{\text{eff}} \cdot D_e)^{1/2}$ values than MFI-TPA samples (Figure 2b, Table 2, main text), and the lower DFT-predicted k_{eff} values for H⁺ sites in channels than in intersections imply that D_e values are higher for MFI-DABCO compared to MFI-TPA. We surmise that different intrapore diffusion resistances should manifest as detectable changes in product distributions on MFI-DABCO and MFI-TPA at otherwise equivalent reaction conditions (gas-phase propene pressure and temperature). To provide the most direct comparison of catalytic behavior, we evaluated the product distribution on MFI-DABCO-3.3 and MFI-TPA-0.33 at 503 K and 16 kPa C₃H₆ (Figure S54), which are conditions that led to equivalent propene conversion (~0.4%) and steady-state dimerization rates (Figure 1, main text), despite the order-of-magnitude larger crystallites for MFI-DABCO than MFI-TPA.

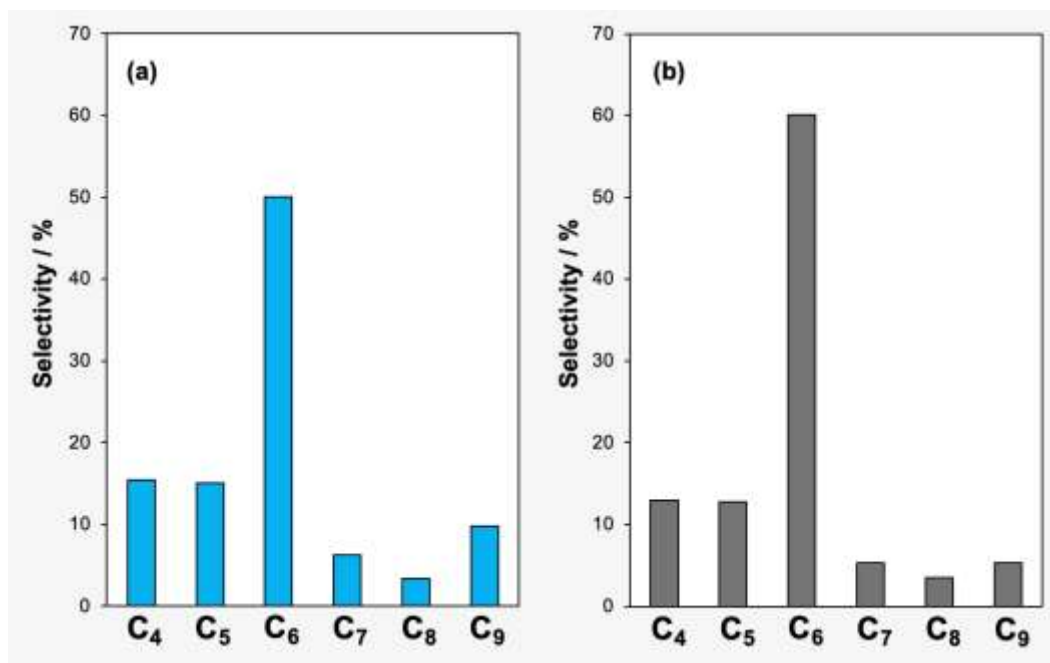


Figure S56. Representative product distribution for propene oligomerization reactions at iso-conversion ($X \sim 0.4\%$) measured at 503 K and 16 kPa C₃H₆ on (a) MFI-DABCO-3.3 and (b) MFI-TPA-0.33. Products are represented by carbon number n as C _{n} .

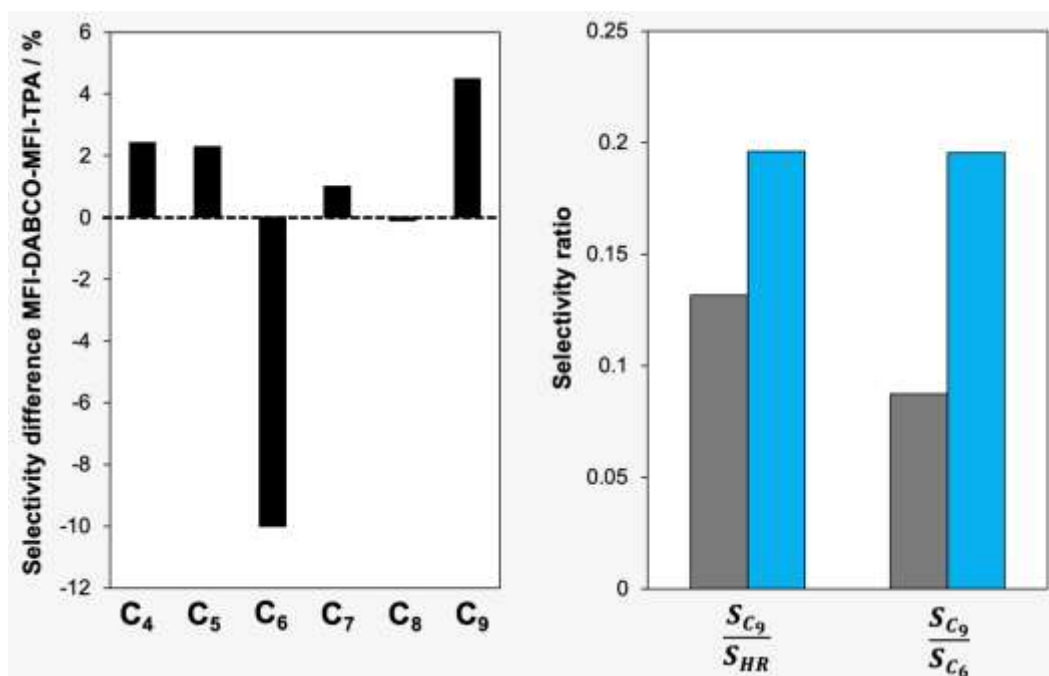


Figure S57. a) Selectivity difference between MFI-DABCO-3.3 and MFI-TPA-0.33 in Figure S54 (16 kPa C₃H₆, 503 K, X~0.4%). b) The ratio of selectivity of trimers to higher rank products (S_{C_9}/S_{HR}) and the selectivity ratio of trimer to dimers (S_{C_9}/S_{C_6}) for MFI-DABCO-3.3 and MFI-TPA-0.33 (16 kPa C₃H₆, 503 K, X~0.4%).

Differences in product distributions are more easily visualized by calculating the product selectivity on MFI-DABCO-3.3 relative to than on MFI-TPA-0.33 (Figure S55a). MFI-DABCO shows ~10% lower selectivity to dimer (i.e., C₆) products compared to MFI-TPA, and higher selectivity to higher-rank products (i.e., C₄, C₅, C₇, C₈, C₉). These measurable differences in the selectivity of gas-phase products that egress from the two types of MFI crystallites indicate that there are changes in the composition of heavier products occluded within MFI micropores during catalysis; yet, the diffusion barriers imposed by these occluded heavier products prevent equilibration between intraporous and gaseous phases, precluding more definitive conclusions regarding the specific composition of these intrapore hydrocarbons. Moreover, the selectivity toward trimer (i.e., C₉) products within higher-rank products and relative to dimer (i.e., C₆) products (Figure S55b) is higher for MFI-DABCO than MFI-TPA, suggesting that heavier oligomer products more readily egress from zeolite crystallites before undergoing β -scission events, implying higher D_e values and weaker intrapore diffusion resistances in MFI-DABCO.

Taken together, these measurable changes in product selectivity on MFI-DABCO and MFI-TPA, at iso-conversion and iso-rate conditions, imply that shifting H⁺ site distributions toward smaller channel environments (characteristic of MFI-DABCO) result in changes in the composition of occluded intrapore hydrocarbons during steady-state catalysis. The specific shifts observed in product distributions would be consistent with higher D_e values in MFI-DABCO, which allow for the more facile egression of larger trimer products prior to their further reaction via beta-scission reactions to form smaller fragments that subsequently egress from MFI crystallites.

References

- (1) Bickel, E. E.; Lee, S.; Gounder, R. Influence of Brønsted Acid-Site Density on Reaction-Diffusion Phenomena That Govern Propene Oligomerization Rate and Selectivity in MFI Zeolites. *ACS Catal.* **2023**, *13* (2), 1257–1269. <https://doi.org/10.1021/acscatal.2c05184>.
- (2) Kim, K.; Ryoo, R.; Jang, H.-D.; Choi, M. Spatial Distribution, Strength, and Dealumination Behavior of Acid Sites in Nanocrystalline MFI Zeolites and Their Catalytic Consequences. *J. Catal.* **2012**, *288*, 115–123. <https://doi.org/10.1016/j.jcat.2012.01.009>.
- (3) Hur, Y. G.; Kester, P. M.; Nimlos, C. T.; Cho, Y.; Miller, J. T.; Gounder, R. Influence of Tetrapropylammonium and Ethylenediamine Structure-Directing Agents on the Framework Al Distribution in B–Al–MFI Zeolites. *Ind. Eng. Chem. Res.* **2019**, *58* (27), 11849–11860. <https://doi.org/10.1021/acs.iecr.9b01726>.
- (4) Kester, P. M.; Miller, J. T.; Gounder, R. Ammonia Titration Methods To Quantify Brønsted Acid Sites in Zeolites Substituted with Aluminum and Boron Heteroatoms. *Ind. Eng. Chem. Res.* **2018**, *57* (19), 6673–6683. <https://doi.org/10.1021/acs.iecr.8b00933>.
- (5) Nimlos, C. T.; Hoffman, A. J.; Hur, Y. G.; Lee, B. J.; Di Iorio, J. R.; Hibbitts, D. D.; Gounder, R. Experimental and Theoretical Assessments of Aluminum Proximity in MFI Zeolites and Its Alteration by Organic and Inorganic Structure-Directing Agents. *Chem. Mater.* **2020**, *32* (21), 9277–9298. <https://doi.org/10.1021/acs.chemmater.0c03154>.
- (6) Bickel, E. E.; McGinness, H.; Zamiechowski, N.; Gounder, R. Synthetic Methods to Vary Crystallite Properties of TON Zeolites and Their Consequences for Brønsted-Acid Catalyzed Propene Oligomerization. *J. Catal.* **2023**, *426*, 189–199. <https://doi.org/10.1016/j.jcat.2023.07.008>.
- (7) Treacy, M. M. J.; Higgins, J. B. Tetrapropylammonium ZSM-5. In *Collection of Simulated XRD Powder Patterns for Zeolites*; Elsevier, 2007; pp 276–277. <https://doi.org/10.1016/B978-044453067-7/50603-1>.
- (8) Ezenwa, S.; Montalvo-Castro, H.; Hoffman, A. J.; Loch, H.; Attebery, J.; Jan, D.-Y.; Schmithorst, M.; Chmelka, B.; Hibbitts, D.; Gounder, R. Synthetic Placement of Active Sites in MFI Zeolites for Selective Toluene Methylation to *Para*-Xylene. *J. Am. Chem. Soc.* **2024**, *146* (15), 10666–10678. <https://doi.org/10.1021/jacs.4c00373>.
- (9) Baerlocher, C.; McCusker, L. B. *Database of Zeolite Structures*. https://america.iza-structure.org/IZA-SC/ftc_table.php (accessed 2022-08-01).
- (10) van Koningsveld, H. High-Temperature (350 K) Orthorhombic Framework Structure of Zeolite H-ZSM-5. *Acta Crystallogr. B* **1990**, *46* (6), 731–735. <https://doi.org/10.1107/S0108768190007522>.